The Ca isotope composition of mare basalts as a probe into the heterogeneous lunar mantle

Martijn Klaver[1]*, Tu-Han Luu[1,2], Jamie Lewis[1], Maximiliaan N. Jansen[3], Mahesh Anand[4], Johannes Schwieters[5] and Tim Elliott[1]

[1]Bristol Isotope Group, School of Earth Sciences, University of Bristol. Wills Memorial Building, Queen's Road, Bristol BS8 1RJ, United Kingdom

[2]Université de Paris, Institut de Physique du Globe de Paris. CNRS, F-75005 Paris, France

[3]School of Earth and Environmental Sciences, Cardiff University. Main Building, Park Place, Cardiff CF10 3AT, United Kingdom

[4]School of Physical Sciences, The Open University. Walton Hall, Milton Keynes MK7 6AA, United Kingdom

[5]Thermo-Fisher Scientific. Hannah-Kunath Strasse, Bremen, Germany

*corresponding author currently at: Institut für Mineralogie, Westfälische Wilhelms-Universität Münster, Corrensstrasse 24, 48149 Münster, Germany; klaverm@uni-muenster.de

ABSTRACT

The Ca isotope compositions of mare basalts offer a novel insight into the heterogeneous nature of the lunar mantle. We present new high-precision Ca isotope data for a suite of low-Ti and high-Ti mare basalts obtained using our collision cell MC-ICP-MS/MS instrument, Proteus. Mare basalts were found to have a Ca isotope composition resembling terrestrial basalts ($\delta^{44/40}Ca_{SRM\ 915a}$ = 0.78–0.89‰) even though they are derived from a differentiated, refractory cumulate mantle source. Modelling of Ca isotope fractionation during crystallisation of a lunar magma ocean (LMO) indicates that the dominantly harzburgitic cumulates of the lunar interior should be isotopically heavier than the Earth's mantle ($\delta^{44/40}Ca_{SRM\ 915a}$ = 1.1–1.2‰ versus 0.93‰, respectively). These are balanced by an isotopically light lunar anorthosite crust, consistent with data for lunar anorthosite and feldspathic breccia meteorites.

We investigate the major element and Ca isotope composition of partial melts of various cumulate reservoirs by combining pMELTS models with equilibrium isotope fractionation mass balance calculations. The principal finding is that harzburgite cumulates alone are too refractory a source to produce low-Ti magmas. Partial melts of harzburgite cumulates have too low CaO contents, too high Al_2O_3/CaO and too high $\delta^{44/40}Ca_{SRM\ 915a}$ to resemble low-Ti magmas. From Ca isotope constraints, we find that the addition of 10–15% of late-stage, clinopyroxenite cumulates crystallising at 95% LMO solidification is required to produce a suitable source that can generate low-Ti basalt compositions. Despite the addition of such late-stage cumulates, pMELTS finds that these hybrid sources are undersaturated in clinopyroxene and are thus consistent with experimental constraints that the mantle sources of the lunar magmas are clinopyroxene-free. High-Ti basalts have slightly lower $\delta^{44/40}Ca_{SRM\ 915a}$ (0.80–0.86‰) than low-Ti magmas (0.85–0.89‰) and clearly elevated TiO_2/CaO. No suitable hybrid source involving ilmenite-bearing cumulates (IBC) was found that could reproduce melts with appropriate $\delta^{44/40}$Ca and major element systematics. Instead, we suggest that metasomatism of low-Ti mantle sources by IBC melts is the most plausible way to generate high-Ti magma sources and the rich diversity in TiO_2 contents of lunar basalts and pyroclastic glasses.

KEYWORDS: Moon; lunar magma ocean; mass-dependent Ca isotope variations; cumulate remelting; ilmenite-bearing cumulates

1. Introduction

One of the main findings of the Apollo programme was that the lunar crust consists predominantly of almost pure anorthosite. This observation spurred a paradigm shift from the pre-Apollo viewpoint of subsolidus accretion of the Moon to the realisation that the lunar crust could represent a flotation cumulate of a crystallising global lunar magma ocean (LMO; Smith et al., 1970; Wood et al., 1970; Warren, 1985). The notion of a magma ocean stage early in the history of the Moon has stood its ground since, and recent geochemical arguments and thermodynamic modelling favour a hot accretion scenario in which the Moon was initially fully molten (e.g., Lock et al., 2018; Steenstra et al., 2020). The Moon is believed to have a differentiated mantle that consists of diverse cumulate lithologies that precipitated during equilibrium and fractional crystallisation of the LMO. The crystallisation sequence of the LMO has been extensively investigated (e.g., Snyder et al., 1992; Elardo et al., 2011; Elkins-Tanton et al., 2011; Lin et al., 2017; Charlier et al., 2018; Rapp and Draper, 2018) and its liquid line of descent is fairly well understood. Olivine and orthopyroxene are the sole phases to crystallise up to 70–80% LMO solidification. Plagioclase is the next phase to saturate, followed by clinopyroxene and in the last 2–5% of crystallisation, ilmenite and quartz. Radiometric dating of the anorthosite crust and radiogenic isotope constraints indicate that LMO solidification and internal differentiation of the Moon was achieved within ca. 200 Ma of its formation (e.g., Borg et al., 2015; Snape et al., 2016; Thiemens et al., 2019).

Subsequent partial melting of the differentiated cumulate mantle gave rise to a suite of extrusive volcanic rocks, the mare basalts, that are predominantly present in large impact basins on the lunar nearside. Like terrestrial basalts, the mare basalts provide a window into the composition of their mantle sources and, as such, provide key evidence on the processes that shaped the internal structure of the Moon. The mare basalts display a rich compositional diversity that far exceeds that of their terrestrial counterparts. Notably, TiO_2 concentrations vary by almost two orders of magnitude in primitive lunar glasses (Delano, 1986; Shearer and Papike, 1993) and constitute the most distinctive geochemical characteristic of lunar basalts recovered in the Apollo missions. The latter display a roughly bimodal distribution in TiO_2 contents, although remote sensing data suggest a continuum in TiO_2 concentrations exists in the mare basalts (e.g., Giguere et al., 2000). To a first order, this compositional heterogeneity of the mare basalts is consistent with remelting of distinct cumulate reservoirs in the lunar mantle. For instance, the most evolved, ilmenite-bearing cumulates (IBC) are commonly linked to the generation of high-Ti magmas (e.g., Ringwood and Kesson, 1976). A persistent complication is that no single cumulate reservoir can be tied directly to any of the known basalt types. In addition, primitive lunar glasses encompassing a wide range in TiO_2 contents are multiply saturated in olivine and orthopyroxene at roughly the same pressure (ca. 2.0 GPa or 400–500 km) and hence appear to be derived from the same depth (e.g., Chen et al., 1982; Elkins-Tanton et al., 2003; Krawczynski and Grove, 2012; Barr and Grove, 2013). Gravitational overturn of the dense IBC provides a mechanism to transport evolved cumulates to greater depths and mix cumulate reservoirs (e.g., Ringwood and Kesson, 1976; Hess and Parmentier, 1995), adding another layer of complexity to the geochemical and mineralogical composition of the source regions of the mare basalts.

Equilibrium isotope fractionation of refractory lithophile elements during crystallisation of the LMO and subsequent remelting is governed by the mineral-melt isotopic fractionation factors of the phases present in the solid residue. As such, mass-dependent isotope systematics of mare basalts can provide insights into the mineralogy and composition of their source regions and this has been explored for elements such as Fe and Ti (e.g., Sossi and Moynier, 2017; Kommescher et al., 2020). Here we focus on Ca, a refractory lithophile element that holds promise as a tracer of lunar differentiation. Based on *ab initio* studies of inter-mineral Ca isotope fractionation, crystallisation of the LMO is predicted to result in a notably different Ca isotope compositions of the different cumulate reservoirs (Huang et al., 2019). By analogy, Ca isotope fractionation occurs during melting of the terrestrial mantle (Figure 1) and a large variation in the Ca isotope composition of mantle residua is observed, although this might in part be attributable to subsolidus metasomatism (e.g., Kang et al., 2017; Antonelli and Simon, 2020; Chen et al., 2020). As such, the Ca isotope composition of lunar basalts appears to be well suited to interrogate LMO crystallisation models and the composition of the source regions of lunar volcanism. However, few Ca isotope data are available for lunar samples. We expand the current dataset by measuring 14 Apollo mare basalt samples for their Ca isotope composition, taking advantage of the analytical advances offered by our prototype collision-cell MC-ICP-MS/MS instrument Proteus. The studied samples

comprise seven low-Ti basalts, six high-Ti basalts and one KREEP-rich basalt (15386). Selection is biased towards low-K varieties to avoid the complexity posed by shallow assimilation of KREEP-rich lithologies.

2. Analytical techniques

The main impediment to high-precision Ca isotope composition measurement by MC-ICP-MS is the high-intensity $^{40}Ar^{+}$ ion beam, meaning that conventionally only the minor isotopes of Ca can be measured. We resolve this problem by using Proteus, a prototype collision-cell MC-ICP-MS/MS instrument developed by Thermo-Fisher Scientific in collaboration with the University of Bristol (see Bevan et al., 2021). The use of He and H_2 as collision and reaction gasses in the collision cell causes near-quantitative elimination of Ar^{+}, thus allowing direct measurement of the $^{40}Ca^{+}$ ion beam. A detailed description of Proteus and the analytical procedures is given in the supplementary material.

We report both the mass-dependent deviation from reference material NIST SRM 915a ($\delta^{44/40}Ca_{SRM\ 915a}$; hereafter abbreviated to $\delta^{44/40}Ca$), measured with the aid of a ^{42}Ca–^{43}Ca double spike, and the radiogenic Ca anomaly reported as $\Delta'_{42/44}{}^{40/44}Ca_{SRM\ 915a}$ (hereafter abbreviated to $\Delta'^{40/44}Ca$), which is the deviation in $^{40}Ca/^{44}Ca$ relative to NIST SRM 915a following exponential-law internal normalisation to $^{42}Ca/^{44}Ca = 0.31221$. Repeat measurements of various reference materials yield a pooled intermediate precision of ±0.034‰ for $\delta^{44/40}Ca$ (2s, n = 84; see supplementary Figure S2) and ±0.049‰ for $\Delta'_{42/44}{}^{40}Ca_{SRM\ 915a}$ (2s, n = 225; see supplementary Figure S3), which we take as the best estimate of the uncertainty on our measurements and show as error bars in all figures. A detailed discussion of uncertainties is provided in the supplementary material. The low-Ti and high-Ti lunar samples have indistinguishable $\Delta'^{40/44}Ca$ relative to the BSE and hence no radiogenic correction needs to be applied to the $\delta^{44/40}Ca$ data. KREEP-rich basalt 15386 has a slight radiogenic $\Delta'^{40/44}Ca$ anomaly for which we apply a correction of +0.055‰ on $\delta^{44/40}Ca$.

Table 1. The Ca isotope composition of the mare basalts.

Sample	CaO* wt.%	Al_2O_3/ CaO*	TiO_2/ CaO*	$\Delta'_{42/44}{}^{40/44}Ca_{SRM\ 915a}$ ‰	2 se	n	$\delta^{44/40}Ca_{SRM\ 915a}$ ‰	2 se	n
low-Ti basalts									
12040.206	8.37	0.93	0.33	-0.003	0.014	16	0.867	0.007	20
12051.229	8.61	0.84	0.36	n.d.			0.846	0.008	20
12052.39	8.68	0.87	0.29	-0.023	0.012	16	0.873	0.007	20
12064.138	9.06	0.88	0.29	-0.019	0.012	16	0.867	0.008	19
14053.260	9.29	1.13	0.21	-0.030	0.018	8	0.887	0.010	17
15016.223	8.12	0.86	0.22	0.002	0.013	16	0.883	0.010	20
15555.982	9.23	1.00	0.10	-0.046	0.012	8	0.872	0.010	15
high-Ti basalts									
10020.232	9.05	0.81	1.10	-0.009	0.013	16	0.861	0.008	20
10050.168	9.43	0.84	1.02	-0.021	0.017	6	0.828	0.015	20
10058.254	9.51	0.83	1.04	n.d.			0.824	0.007	16
70215.326	8.97	0.77	1.24	n.d.			0.799	0.007	16
74275.323	9.28	0.79	1.20	-0.007	0.011	16	0.838	0.007	20
75055.49	9.68	0.81	1.17	-0.053	0.018	8	0.800	0.009	20
KREEP-rich basalt									
15386.54	8.34	1.47	0.20	0.030	0.015	8	0.774	0.009	17

*The 2se uncertainty quoted in the table is the two standard error of the mean for the number of replicate measurements. We use the pooled 2s intermediate precision of reference materials (0.034‰ for $\delta^{44/40}Ca$, 0.049‰ for $\Delta'^{40/44}Ca$; see supplementary material for details) as the best estimate of the uncertainty on the Ca isotope compositions of the lunar samples. *Corrected for low-pressure fractional crystallisation; see main text and supplementary material.*

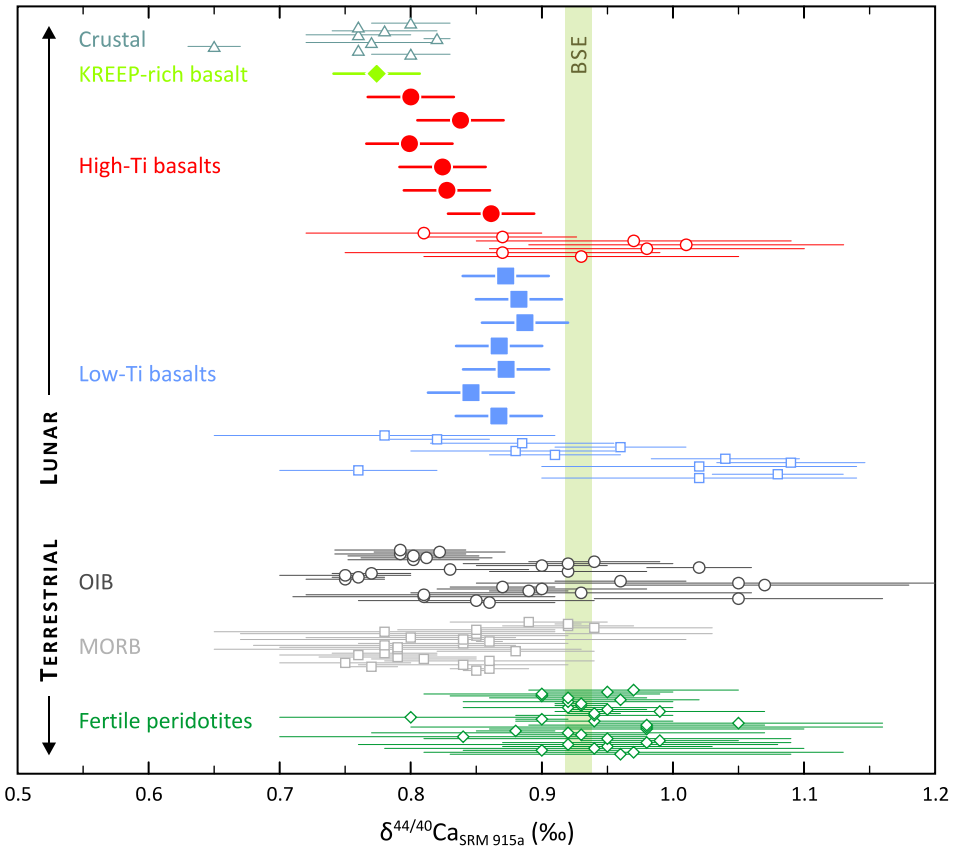

Figure 1. *New $\delta^{44/40}Ca$ data for the mare basalts (solid symbols); open symbols depict previously reported Ca isotope composition of samples recovered by the Apollo missions and lunar meteorites (Simon and DePaolo, 2010; Valdes et al., 2014; Simon et al., 2017; Schiller et al., 2018; Wu et al., 2020). The crustal samples comprise feldspathic breccias and anorthosites. See supplementary material for a more detailed comparison of data from this study with published values. The Ca isotope composition of the terrestrial fertile mantle (lherzolites with ≥2.5 wt.% CaO), mid-ocean ridge basalts (MORB) and ocean island basalts (OIB) is shown for comparison (Huang et al., 2011; Jacobson et al., 2015; Kang et al., 2017; Zhu et al., 2018; Chen et al., 2019; Chen et al., 2020). The green bar is the average of the fertile lherzolites ($\delta^{44/40}Ca$ = 0.928 ± 0.010‰; 95% confidence interval), which we use as the best estimate of the composition of the bulk silicate Earth (BSE; cf., Antonelli and Simon, 2020).*

3. Results

The Ca isotope composition data for the lunar samples are provided in Table 1 and shown in Figure 1. The low- and high-Ti basalts have no discernible radiogenic or nucleosynthetic ^{40}Ca anomaly compared to terrestrial basalts and, by implication, the Earth (see supplementary Figure S4). Conversely, KREEP-rich basalt 15386 has distinctly positive $\Delta'^{40/44}Ca$, consistent with its elevated K/Ca and 3.9 Ga radiogenic ingrowth. In mass-dependent Ca isotope space, the low-Ti basalts form a homogeneous population ($\delta^{44/40}Ca$ = 0.87 ± 0.03‰; 2s) whereas the high-Ti basalts are more heterogeneous and tend towards isotopically lighter compositions ($\delta^{44/40}Ca$ = 0.80–0.86‰). Although there is only a subtle difference between the two, a Student's T-test indicates that the low-Ti and high-Ti populations are statistically distinct (p = 0.003). The total variation in $\delta^{44/40}Ca$ of the new mare basalt measurements is significantly smaller than the range reported in the literature (Figure 1). Importantly, our average for low-Ti basalts agrees very well with data reported by Valdes et al. (2014), Schiller et al. (2018) and Wu et al. (2020). In contrast, low-Ti basalts measured by Simon and DePaolo (2010) and Simon et al. (2017) are systematically offset to higher $\delta^{44/40}Ca$ by ca. 0.1 ‰. The potential causes and implications of this dichotomy are discussed in detail in the supplementary material, but we infer that it is rooted a bias introduced by renormalisation of their data to SRM 915a.

4. Discussion

4.1. Ca isotope fractionation during lunar magma ocean solidification

Crystallisation of the LMO is predicted to induce significant mass-dependent Ca isotope fractionation between various cumulate reservoirs and the residual melt (Huang et al., 2019). We have calculated the $\delta^{44/40}$Ca composition of the cumulate pile based on the experimental LMO crystallisation model of Charlier et al. (2018). These authors parameterised the composition of crystallising phases as a function of melt chemistry and intensive parameters, thus enabling forward modelling of LMO crystallisation (see supplementary material for details). As LMO crystallisation likely starts as an equilibrium process and changes to fractional crystallisation at some point during its evolution, we have modelled two scenarios where the equilibrium- to fractional crystallisation transition occurs at 40 or 70% crystallisation, which will be referred to as the fractional crystallisation-dominated (FC) and equilibrium crystallisation-dominated (EC) model, respectively (Figure 2). It should be noted that some studies suggest that fractional crystallisation was dominant from the start of LMO solidification (e.g., Suckale et al., 2012; Rapp and Draper, 2018). For Ca isotope systematics, the style of crystallisation is trivial during the olivine-only stage as Ca is highly incompatible in olivine (D = 0.03; (Charlier et al., 2018). Our FC model can therefore be seen as representative for any scenario in which fractional crystallisation starts during the first 50% of LMO solidification (see supplementary Figure S7).

Equilibrium, mass-dependent isotope fractionation between melt and solid phases during crystallisation or partial melting is governed by the mineral-melt isotope fractionation factors of the phases present in the solid assemblage. The magnitude of these fractionation factors depends on variations in bond strength of an element and is inversely proportional to the square of the temperature. As such, mass-dependent isotope compositions are a powerful tracer of the mineralogy of residua in equilibrium with a melt. In the LMO crystallisation model, the Ca isotope composition of the instantaneous crystallising assemblage and residual melt was calculated through an isotopic mass balance using temperature-dependent mineral-mineral Ca isotope fractionation factors calculated from first principles by Huang et al. (2019), which are tabulated in supplementary Table S3. These are related to the composition of the melt using the empirical augite-melt fractionation factor of Zhang et al. (2018) derived from Kilauea Iki lava lake samples ($\Delta^{44/40}Ca_{aug\text{-}melt}$ = 0.09 ± 0.07‰ at 1000 K), the uncertainty on which is propagated throughout the modelling. Further details and a justification of the use of these isotopic fractionation factors are given in the supplementary material.

The starting composition for the modelling is the lunar primitive upper mantle (LPUM) bulk LMO composition of Longhi (2006), which is slightly volatile element-depleted (Na, K) but otherwise identical to the bulk silicate Earth (BSE). The Ca isotope composition of the bulk Moon is unknown, but as a starting point to our modelling, we assume that the bulk Moon has the same Ca isotope composition as the BSE. The Earth and Moon have an identical nucleosynthetic ^{48}Ca signature whereas planetary buildings blocks display pronounced ^{48}Ca heterogeneity (Schiller et al., 2018). In addition, lunar and terrestrial basalts have indistinguishable $\Delta'^{40/44}$Ca (supplementary Figure S4). In conjunction with the general homogeneity of $\delta^{44/40}$Ca in CAI-free chondritic meteorites (e.g., Valdes et al., 2014; Huang and Jacobsen, 2017), this suggests that either the impactor and proto-Earth had overlapping Ca isotope compositions, or the BSE and Moon achieved complete Ca isotope homogenisation in the aftermath of the giant impact. Given the refractory nature of Ca, it is unlikely that any evaporative fractionation occurred. Hence, we take a weighted average of the fertile lherzolites shown in Figure 1 ($\delta^{44/40}$Ca = 0.928 ± 0.010‰) as representative of the bulk Moon and propagate the uncertainty on this BSE value throughout the modelling. This assertion agrees well with the BSM estimate ($\delta^{44/40}$Ca = 0.89–0.95‰) derived from the measurement of lunar feldspathic and basaltic meteorites proposed by Wu et al. (2020).

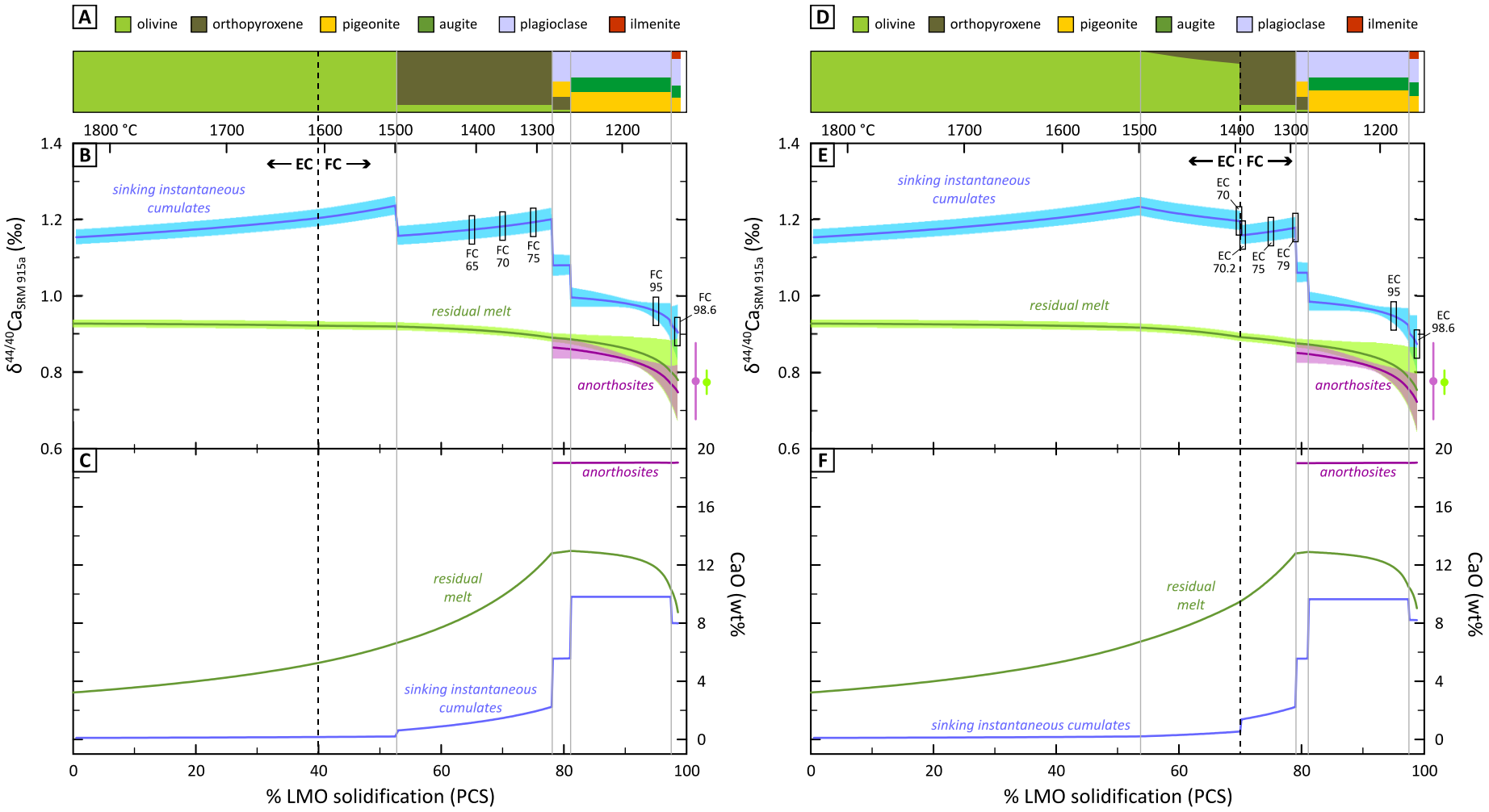
A
olivine
orthopyroxene
pigeonite
augite
plagioclase
ilmenite
1800 °C
1700
1600
1500
1400
1300
1200
B
← EC FC →
sinking instantaneous cumulates
FC 65
FC 70
FC 75
FC 95
FC 98.6
residual melt
anorthosites
δ44/40CaSRM 915a (‰)
1.4
1.2
1.0
0.8
0.6
C
anorthosites
residual melt
sinking instantaneous cumulates
CaO (wt%)
20
16
12
8
4
0
0
20
40
60
80
100
% LMO solidification (PCS)
D
olivine
orthopyroxene
pigeonite
augite
plagioclase
ilmenite
1800 °C
1700
1600
1500
1400
1300
1200
E
← EC FC →
sinking instantaneous cumulates
EC 70
EC 70.2
EC 75
EC 79
EC 95
EC 98.6
residual melt
anorthosites
δ44/40CaSRM 915a (‰)
1.4
1.2
1.0
0.8
0.6
F
anorthosites
residual melt
sinking instantaneous cumulates
CaO (wt%)
20
16
12
8
4
0
0
20
40
60
80
100
% LMO solidification (PCS)

Figure 2. *Lunar magma ocean solidification models for equilibrium crystallisation up to 40% (FC model; panels a–c) and equilibrium crystallisation up to 70% (EC model; panels d–f). The dashed line denotes the transition from equilibrium to fractional crystallisation. (a, d) phase assemblages in equilibrium with the residual melt. (b, e) $\delta^{44/40}$Ca evolution of residual melt, instantaneous sinking cumulates (olivine, pyroxene, and garnet, containing 7 wt.% trapped plagioclase when present as a crystallising phase) and anorthosite crust. The shaded envelopes display the 2s uncertainty that comprises the uncertainty on the bulk Moon composition and the diopside-melt Ca fractionation factor; see main text and supplementary material for more details. The black boxes highlight the composition of cumulate reservoirs used in partial melting modelling in this study; the purple and green markers on the right show the composition of average lunar anorthosites and feldspathic breccias (Schiller et al., 2018; Wu et al., 2020) and KREEP-rich basalt 15386, respectively. (c, f) CaO content of residual melt, instantaneous sinking cumulates and anorthosite crust.*

The results of the LMO crystallisation modelling are depicted in Figure 2 for the FC and EC models, where the variation in $\delta^{44/40}$Ca and CaO content of instantaneous cumulates and the residual melt are shown as a function of percentage LMO crystallisation. Upon plagioclase saturation, the instantaneous cumulates illustrated in Figure 2 comprise the mafic phases that have a higher density than the melt and sink to contribute to the cumulate mantle; the composition of the anorthosites that form the lunar crust is shown separately. In line with previous studies (e.g., Snyder et al., 1992; van Orman and Grove, 2000) we assume that the sinking instantaneous cumulates contain 7% trapped plagioclase. The EC and FC models yield very similar results for the Ca content and $\delta^{44/40}$Ca of residual melt and anorthosite crust. Instantaneous cumulates forming between 50 and 80% crystallisation differ slightly due to the different proportions of orthopyroxene in the crystallising assemblage but overall have similar $\delta^{44/40}$Ca (1.1–1.2‰).

Olivine and orthopyroxene are the sole crystallising phases up to 79% crystallisation. Both phases have a mineral-melt Ca isotope fractionation factor significantly above unity (see supplementary Figure S8). Hence, harzburgite cumulates have a distinctly heavy Ca isotope composition but, due to their low Ca contents, exert little leverage on the $\delta^{44/40}$Ca of the residual melt, which only decreases by ca. 0.03‰ after 79% crystallisation (Figure 2). Clinopyroxene (pigeonite, augite) and plagioclase control the Ca isotope evolution in the last ca. 30% of LMO solidification, causing $\delta^{44/40}$Ca of the residual melt to further decrease to ca. 0.77‰. The last dregs of residual LMO melt are rich in incompatible elements and commonly referred to as the urKREEP reservoir, which plays an important role in the petrogenesis of KREEP-rich basalts. Of the mare basalts measured in this study, the KREEP-rich basalt has lower $\delta^{44/40}$Ca than the non-KREEP basalts and its $\delta^{44/40}$Ca overlaps with the predicted composition of the urKREEP reservoir.

From the LMO crystallisation models, it is apparent that the vast majority of the lunar cumulate mantle is isotopically heavy than the bulk Moon; only the ilmenite-bearing cumulates (IBC; 97.4-99% crystallisation) have marginally lower $\delta^{44/40}$Ca. The isotopically heavy lunar mantle is balanced by a light Ca isotope composition of the Ca-rich anorthosite crust. Feldspathic breccia meteorites and anorthosite grains therein yield an average $\delta^{44/40}$Ca of 0.77 ± 0.10‰ (Figure 1; Schiller et al., 2018; Wu et al., 2020), consistent with the predictions of our LMO crystallisation modelling.

4.2. Mineralogy and composition of low-Ti magma sources

The major element, trace element and radiogenic isotope compositions of the mare basalts cannot be reconciled with melting of a primordial, undifferentiated lunar mantle reservoir. Compared to terrestrial normal mid-ocean ridge basalts (N-MORB), which originate from partial melting of the slightly depleted terrestrial upper mantle, primitive lunar glasses invariably have lower CaO and Al_2O_3 contents (Figure 3). At first glance, this appears to be consistent remelting of a cumulate mantle that was depleted in Ca and Al by the extraction of the anorthosite crust (e.g., Ringwood and Kesson, 1976; Hess, 2000; Shearer et al., 2006). The more refractory nature of the mantle source of mare volcanism is supported by experimental studies, which indicate that mare magmas are multiply saturated in olivine and orthopyroxene, but not in clinopyroxene, at ca. 2 GPa and 1450-1540 °C regardless of their TiO_2 content (e.g., Chen et al., 1982; Longhi, 1992; Elkins-Tanton et al., 2003; Krawczynski and Grove, 2012; Barr and Grove, 2013). Unlike most terrestrial basalts, clinopyroxene (pigeonite or augite) is not present on the liquidus at any pressure and the mare basalts appear to be in equilibrium with a clinopyroxene-free, harzburgitic residual assemblage.

The Ca isotope composition of the mare basalts is ideally suited to constrain which cumulate lithology, or mixture of lithologies, is a suitable source for the mare basalts. We employ pMELTS (version 5.6.1; Ghiorso et al., 2002) to determine the major element composition of low-degree partial melts generated by remelting various cumulate reservoirs (boxes in Figure 2b and e). The $\delta^{44/40}$Ca composition of these partial melts is calculated through an isotopic mass balance that uses the same parameters as those for the LMO crystallisation modelling described in section 4.1. The pMELTS models were run at 2.0 GPa, the average multiple saturation pressure of green pyroclastic glasses (Chen et al., 1982; Elkins-Tanton et al., 2003; Barr and Grove, 2013), and fO_2 = IW. Sensitivity of the melt composition and residual mineral assemblage to pressure and oxygen fugacity was investigated (supplementary Figure S10) but only Al_2O_3/CaO of the melt was found to vary significantly with pressure due to the pressure-dependence of Al partitioning into orthopyroxene. We acknowledge that the lunar cumulate compositions and low fO_2 are near the limits of the experimental calibration of pMELTS, yet the insensitivity of the results to oxygen fugacity provides reassurance that they are robust. In addition, the compositions of residual phases calculated by pMELTS matches those found in experimental multiple saturation studies of lunar pyroclastic glasses. A detailed description of the modelling approach and results is given in the supplementary material.

A final note before discussing the results of the modelling is the modification of the major element and $\delta^{44/40}$Ca composition of the mare basalts after segregation from their mantle source. Mare basalts are not primary melts but variably affected by fractional crystallisation of olivine and, for some high-Ti basalts, armalcolite at low pressure (e.g., Longhi, 1992; see Figure 3). We have applied a correction to the major element composition and $\delta^{44/40}$Ca of the samples in this study to account for the removal of up to 30 wt.% olivine and minor amounts of armalcolite at low pressure, which is described in detail in the supplementary material. This correction has a notable effect on major element concentrations, but key ratios such as $\delta^{44/40}$Ca, Al_2O_3/CaO and TiO_2/CaO are barely affected by the removal of olivine. The magnitude of correction on $\delta^{44/40}$Ca is <0.01% and hence significantly smaller than the analytical uncertainty (0.03‰; see supplementary Figure S6). In the subsequent discussion and figures, low-pressure differentiation-corrected major element and $\delta^{44/40}$Ca compositions are shown.

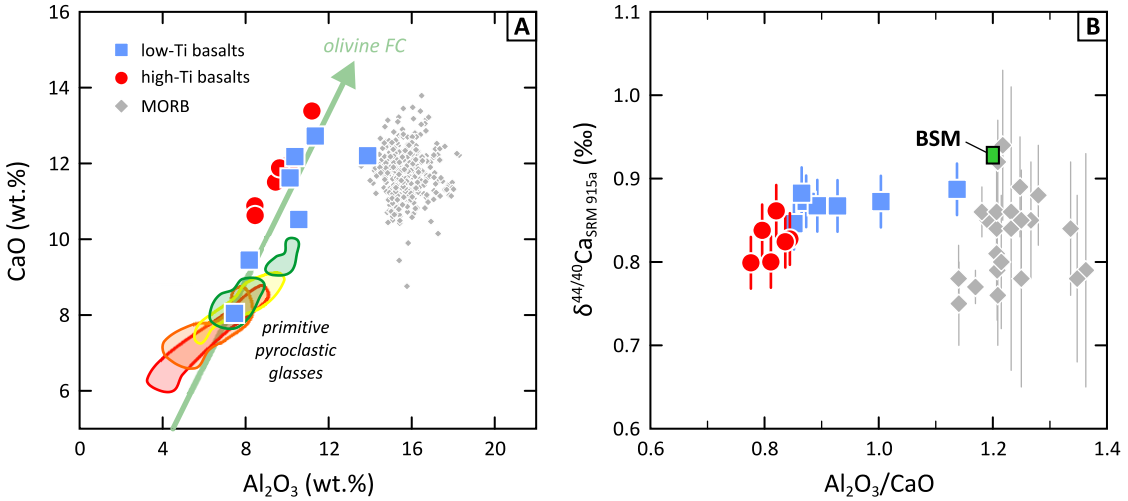

Figure 3. *Composition of the low-Ti and high-Ti basalts in this study in comparison with terrestrial normal mid-ocean ridge basalts (N-MORB). A) Al_2O_3 versus CaO content of the mare basalts (not corrected for low-pressure olivine fractional crystallisation). The shaded fields show the composition of primitive pyroclastic glasses (Delano, 1986; Shearer and Papike, 1993), with TiO_2 content increasing from green to yellow, orange and red glasses. The arrow shows the effect of low-pressure fractional crystallisation of olivine. Primitive N-MORB (Mg# ≥55; La/Sm_{PM} <1.1) are from Arevalo and McDonough (2010). B) Al_2O_3/CaO versus $\delta^{44/40}$Ca for the mare basalts and terrestrial MORB (Zhu et al., 2018; Chen et al., 2020). The bulk silicate Moon (BSM) is the LPUM composition of Longhi (2006) with $\delta^{44/40}$Ca of the bulk silicate Earth (see Figure 1).*

4.2.1. Why harzburgite cumulates alone are not a suitable source

The Ca isotope composition of the mare basalts overlaps with terrestrial oceanic basalts such as MORB and most OIB (Figures 1 and 3), as also noted by Simon et al. (2017). At first glance, this seems reasonable given the presumed identical $\delta^{44/40}$Ca of the Moon and BSE, yet there is a marked complication. Terrestrial basalts are saturated with a lherzolitic or, for some OIBs, pyroxenitic assemblage (i.e., clinopyroxene is present in the melting residue) whereas lunar basalts are interpreted to be produced by remelting of clinopyroxene-free harzburgite cumulates (e.g., Shearer et al., 2006). Low-Ti lunar magmas are undersaturated in clinopyroxene at any pressure, which is pertinent because, by virtue of its high Ca content, clinopyroxene exerts strong leverage on the Ca isotope fractionation factor between the bulk residue and melt. As a result, melts in equilibrium with a lherzolitic, clinopyroxene-rich source would have $\delta^{44/40}$Ca only slightly lower than their source (compare MORB and fertile peridotites in Figure 1; see also Antonelli and Simon, 2020) whereas melts in equilibrium with a clinopyroxene-free source are much more fractionated due to the larger orthopyroxene-melt fractionation factor (see supplementary Figure S8). During fractional crystallisation of the LMO, isotopically heavy Ca is preferentially incorporated in the cumulates and hence the lunar mantle has $\delta^{44/40}$Ca that is >0.2‰ higher than fertile terrestrial peridotites (Figure 2). These two factors could work together in such a way to coincidentally produce mare basalts that resemble the $\delta^{44/40}$Ca of terrestrial basalts, but below we will demonstrate that this cannot be the case.

Harzburgite cumulates form prior to saturation of the LMO residual melt in plagioclase and clinopyroxene, which occurs at 78–79% LMO solidification (Charlier et al., 2018). In the two LMO crystallisation models that are considered in this study, three different suites of harzburgite cumulates can be distinguished (Figure 2). In the EC model, equilibrium crystallisation of the LMO up to 70% produces a homogeneous, high-Mg# harzburgite cumulate that contains ca. 21 wt.% orthopyroxene and constitutes the majority of the lunar mantle (EC70; see Figure 2). Subsequent cotectic fractional crystallisation of olivine and orthopyroxene yields orthopyroxene-dominated (88 wt.%) assemblages (EC70.1–79; see Figure 2). In the FC model, the transition from equilibrium- to fractional crystallisation occurs during the olivine-only stage and no primitive olivine-rich harzburgites are formed. Hence, in the FC model, only orthopyroxene-rich harzburgite cumulates form between 53 and 78% LMO crystallisation (FC53–78; see Figure 2).

The major element and $\delta^{44/40}$Ca composition of low-degree partial melts of these harzburgite reservoirs is shown in Figure 4. Remelting of these harzburgite suites produces melts with relatively similar major element compositions and $\delta^{44/40}$Ca, yet none match the composition of the low-Ti mare basalts. Partial melts have too low CaO contents, too high Al_2O_3/CaO and too high $\delta^{44/40}$Ca (Figure 4) compared to the low-Ti basalts. In the absence of clinopyroxene, Ca is incompatible and partial melting produces residua with very low Ca contents. From mass balance it follows that the partial melts have $\delta^{44/40}$Ca close to that of their source, even though the bulk residue-melt Ca isotope fractionation is larger than for a lherzolitic residual assemblage. In conjunction with the isotopically heavy composition of the harzburgite cumulates compared to the bulk Moon, this explains why remelting of these cumulates will produce basaltic melts with $\delta^{44/40}$Ca that is notably higher than terrestrial lherzolite-saturated oceanic basalts, and the observed composition of the mare basalts.

Only an extremely low degree of melting (<1%) of an EC70 cumulate that contains 2% trapped interstitial residual liquid (TIRL), which has the $\delta^{44/40}$Ca composition of residual melt at the time of 70% LMO crystallisation (ca. 0.90‰; Figure 2) and dominates the Ca budget of that cumulate, produces a melt with $\delta^{44/40}$Ca approaching that of the low-Ti basalts (Figure 4a). Even such a modest proportion of TIRL is, however, at the upper limit of the permissible amount of interstitial melt from a trace element and radiogenic isotope perspective (e.g., Hallis et al., 2014). Moreover, extremely low-degree partial melts of a TIRL-rich source are too enriched in incompatible elements whilst CaO contents are still ca. 30% lower than in the low-Ti basalts (Figure 4a). Hence, we find no plausible scenario in which remelting of harzburgite cumulates alone can reproduce the combined $\delta^{44/40}$Ca and major element composition of the lunar low-Ti magmas. The new $\delta^{44/40}$Ca constraints substantiate previous suggestions that more evolved cumulates or melts of a primordial mantle reservoir need to play a role in the generation of the low-Ti magmas (Hughes et al., 1988; Longhi, 2006; Barr and Grove, 2013; Hallis et al., 2014).

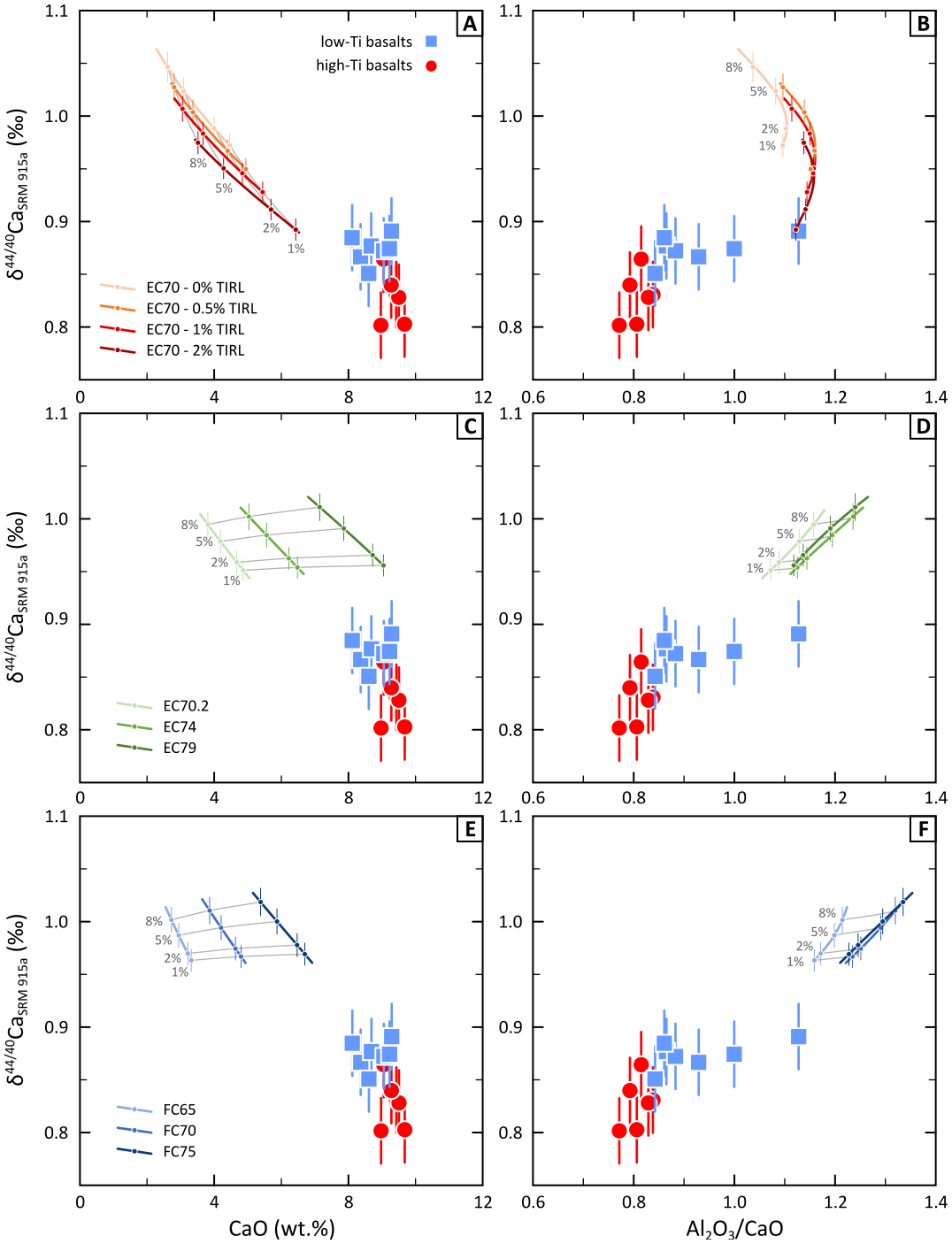

Figure 4. *Major element and $\delta^{44/40}Ca$ composition of the mare basalts compared to partial melting models for harzburgite cumulate reservoirs: CaO versus $\delta^{44/40}Ca$ (panels a, c and e) and Al_2O_3/CaO versus $\delta^{44/40}Ca$ (panels b, d and f). Mare basalt data are corrected for low-pressure fractional crystallisation of olivine±armalcolite (see supplementary Figure S6). Melting models depict 1-8% batch melting (grey lines and labels) of cumulates that crystallised at different degrees of LMO crystallisation for both the EC and FC model (see Figure 2; e.g., EC74 is the cumulate in equilibrium with the melt at 74% LMO solidification in the EC model). For the EC70 cumulate, which is the harzburgite cumulate formed by 70% equilibrium crystallisation of the LMO, partial melts are shown for a variable proportion of trapped interstitial residual liquid (TIRL) that can be present in the cumulate. Error bars ($\delta^{44/40}Ca$) for the melting model incorporate the uncertainty on the bulk Moon composition and the diopside-melt Ca isotope fractionation factor; see text and supplementary material for details.*

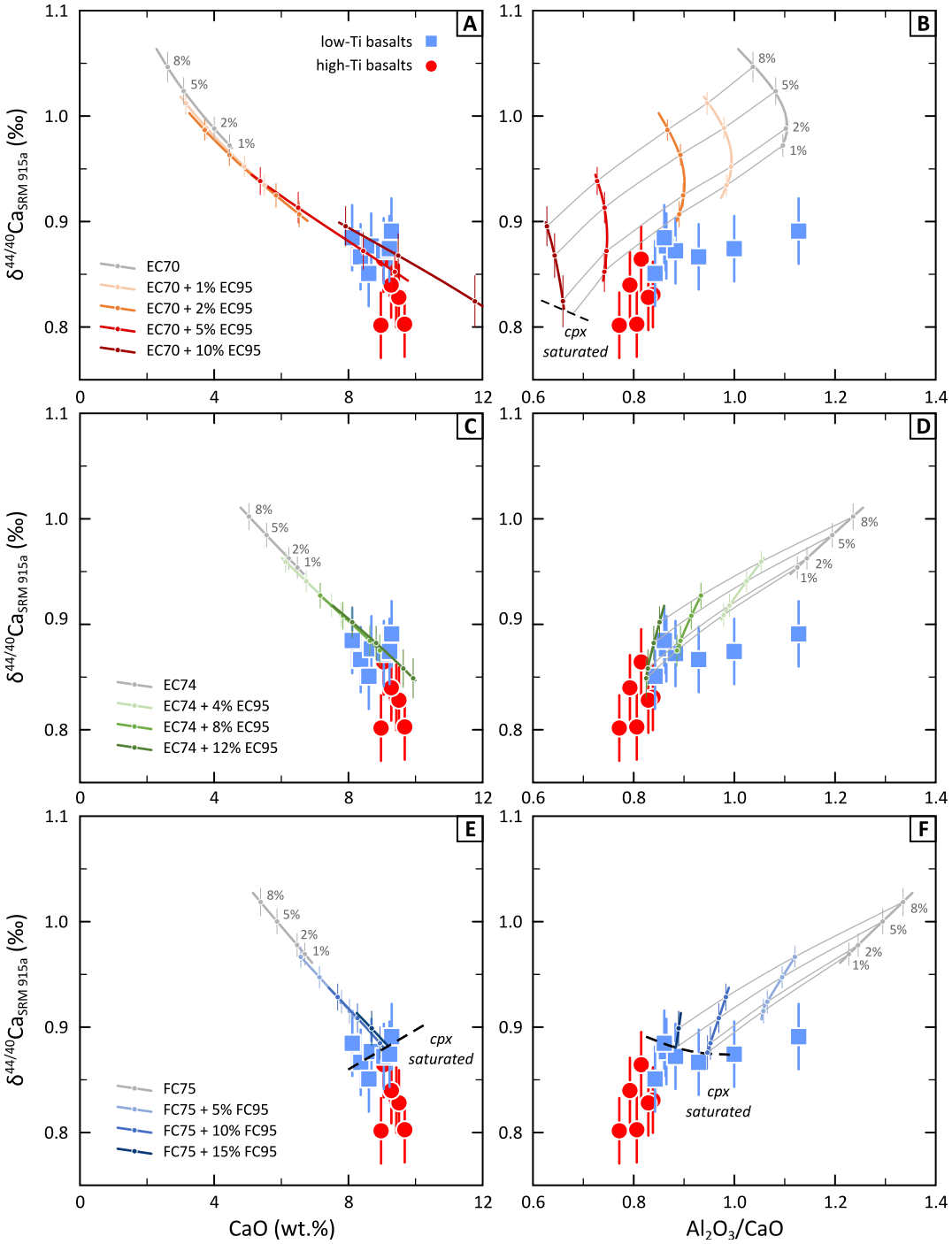

Figure 5. *Major element and $\delta^{44/40}Ca$ composition of the mare basalts compared to partial melting models for hybrid cumulate reservoirs where late-stage (95% LMO crystallisation) clinopyroxenite cumulates are mixed with harzburgite cumulate reservoirs: CaO versus $\delta^{44/40}Ca$ (panels a, c and e) and Al_2O_3/CaO versus $\delta^{44/40}Ca$ (panels b, d and f). Mare basalt data are corrected for low-pressure fractional crystallisation of olivine±armalcolite (see supplementary Figure S6). Melting models depict 1-8% batch melting (grey lines and labels) of hybrid cumulate reservoirs for both the EC model and FC model (see Figure 2; e.g., EC74 is the instantaneous cumulate crystallising at 74% LMO solidification in the EC model). The black dashed line indicates where partial melts become saturated in high-Ca pyroxene according to the pMELTS models. Error bars ($\delta^{44/40}Ca$) for the melting model incorporate the uncertainty on the bulk Moon composition and the diopside-melt Ca isotope fractionation factor; see text and supplementary material for details.*

4.2.2. The crucial role of clinopyroxenite cumulates in low-Ti magma petrogenesis

A Ca-rich component with low $\delta^{44/40}$Ca apparently has to be added to the harzburgite cumulates to produce a more suitable, hybrid cumulate source for the low-Ti basalts. Late-stage clinopyroxene-rich, but ilmenite-free, cumulates that form in the interval of ca. 81–97% LMO solidification could form this low-$\delta^{44/40}$Ca component. Any hybrid cumulate source composition, however, has to satisfy the experimental constraint that clinopyroxene is not a residual phase in the source of low-Ti magmas (e.g., Longhi, 1992; Elkins-Tanton et al., 2003; Barr and Grove, 2013). We investigate whether hybrid cumulates, formed through mixing of harzburgite cumulate reservoirs with small proportions of late-stage clinopyroxenite cumulates can form an appropriate mantle source.

Modelling with pMELTS suggests that orthopyroxene has the capacity to incorporate significant proportions of a clinopyroxene component in its crystal structure at high pressure and temperature (2.0 GPa and >1500 °C), as previously hypothesized by Shearer et al. (2006). It was found that hybrid cumulate reservoirs can contain up to 15 wt.% of late-stage clinopyroxenite cumulates formed at 95% LMO solidification (FC95 and EC95) without becoming saturated in clinopyroxene. In some cases, clinopyroxene (augite or pigeonite) is present as a solidus phase but is exhausted after a few percent of melting (Figure 5). Partial melting of these hybrid cumulates produces melts that are undersaturated in clinopyroxene and have higher CaO content, lower Al_2O_3/CaO and lower $\delta^{44/40}$Ca than partial melts of pure harzburgite cumulates sources (Figure 5). Both Al_2O_3/CaO and $\delta^{44/40}$Ca are negatively correlated with the proportion of clinopyroxenite incorporated into the hybrid cumulates.

No hybrid composition containing EC70 cumulates (the harzburgites with ca. 21 wt.% orthopyroxene that formed after 70% equilibrium crystallisation of the LMO) can generate partial melts that match the composition of low-Ti lunar magmas; partial melts that have appropriate Al_2O_3/CaO and $\delta^{44/40}$Ca still have too low CaO contents (ca. 6 wt.%; see Figure 5a). The more evolved, orthopyroxene-rich harzburgite cumulates that are present in both the FC and EC model, however, can form suitable sources for the low-Ti magmas when mixed with late-stage cumulates (Figure 5c–f). For the EC model, a hybrid source consisting of 8–12 wt.% of late-stage EC95 cumulates mixed with an EC74 harzburgite cumulate can produce partial melts with 8–9 wt.% CaO, Al_2O_3/CaO between 0.8 and 0.9 and $\delta^{44/40}$Ca of ca. 0.88, which are a good match to most low-Ti mare basalts. Neither augite nor pigeonite is present as a solidus phase for these hybrid compositions, thus satisfying the constraints imposed by multiple saturation experiments. Hybrid sources in the FC model can also produce partial melt compositions that match the low-Ti basalts (Figure 5e–f) but require the addition of a larger proportion of late-stage FC95 cumulates (15 wt.%). The pMELTS models indicate that such hybrid cumulates have pigeonite (6–7 wt.% CaO) as a solidus phase. Pigeonite is, however, exhausted after ca. 5% melting and hence larger degree partial melts of such a hybrid cumulate do satisfy the absence of residual clinopyroxene criterion.

Additional support for the involvement of late-stage, clinopyroxene-bearing cumulates comes from rare earth element (REE) systematics of the low-Ti mare basalts. The low-Ti basalts are characterised by a positive light REE slope, negative heavy REE slope and negative Eu anomaly; a signature that cannot be produced by melting of harzburgite cumulates precipitated prior to saturation of the LMO residual melt in plagioclase (e.g., Hughes et al., 1988; Hallis et al., 2014). The residual melt from which the late-stage cumulates crystallise has elevated REE contents, caused by the segregation of >80% olivine and orthopyroxene, and a negative Eu anomaly imparted by the strong affinity of Eu^{2+} for plagioclase under the highly reducing conditions of the Moon. Clinopyroxene will thus be relatively REE-rich with a convex-up REE pattern and a pronounced negative Eu anomaly as a combined result of low Eu contents in the residual melt and low partition coefficient for Eu^{2+} in clinopyroxene. When clinopyroxenite cumulates are mixed into the harzburgites, the REE contents of the former overwhelm the small amount of REE present in the harzburgite cumulates. Hybrid cumulate reservoirs thus effectively mirror the REE patterns of the clinopyroxenites and, upon remelting of the hybrid cumulates, will impart their REE signature onto the low-Ti magmas.

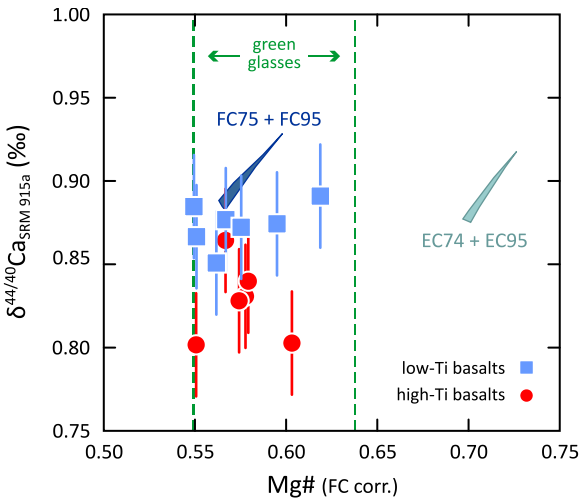

Figure 6. *Low-pressure fractionation corrected Mg# (molar Mg/[Mg+Fe]) versus $\delta^{44/40}$Ca of the lunar mare basalts. Model compositions for the composition of clinopyroxene-undersaturated, 1-8% partial melts of hybrid cumulate sources that satisfy the criteria of 7.5-9.0 wt.% CaO and Al_2O_3/CaO between 0.8 and 1.0 are shown as shaded fields for the EC and FC model. These hybrid cumulate sources contain 8-12 and 10-15 wt.% clinopyroxene-rich cumulates formed at 95% LMO crystallisation, respectively. The green dashed lines indicate the range in Mg# of primitive low-Ti (green) pyroclastic glasses (excluding the anomalous Apollo 15 type C glasses; Delano, 1986; Shearer and Papike, 1993).*

4.2.3. The transition from equilibrium- to fractional crystallisation

Both LMO solidification scenarios investigated here (EC and FC model) produce cumulate assemblages that can generate low-Ti basalts-like compositions upon mixing and remelting. Hence Ca isotope systematics cannot be used to differentiate between an early (FC model) and late (EC model) transition from equilibrium- to fractional crystallisation. The two models, however, predict markedly different Mg# (molar Mg/([Mg+Fe]) of the cumulate source regions and, by implication, the Mg# of partial melts that could be generated from such sources. Protracted equilibrium crystallisation (up to 70% LMO solidification in the EC model) causes the Mg# of the residual melt to be continuously buffered by the cumulate pile. As a result, harzburgite cumulates in this model are far too magnesian to be an appropriate source to the low-Ti magmas (Hess, 2000). In contrast, early segregation of high-Mg# cumulates in the FC model drives a more rapid decrease in Mg# of the residual melt. Partial melts of hybrid cumulate sources in the EC and FC models can thus have overlapping Ca elemental and isotope compositions, but FC model melts have notably lower Mg# than EC model melts (ca. 0.57 versus ca. 0.71, respectively; Figure 6). The Mg# of melts in the EC model is notably higher than that of any of the primitive pyroclastic glasses and the low-pressure fractionation corrected Mg# of the low-Ti basalts in this study, whereas the composition of FC model melts provides a better match with these. Hence, our modelling suggests that, for an LPUM bulk Moon composition (Longhi, 2006), an earlier rather than late transition to fractional crystallisation is more compatible with the Mg# of the low-Ti lunar magmas. A similar conclusion was reached by Hess (2000), which is consistent with evidence from fluid dynamics that indicates that early crystal fractionation during LMO solidification is required to efficiently separate plagioclase to form the lunar crust (Suckale et al., 2012).

4.2.4. High-Al basalts and the variation in Al_2O_3/CaO

A major element feature that is not well reproduced in our hybrid source model for low-Ti magmas, is the range in Al_2O_3/CaO displayed by the low-Ti samples, notably high-Al basalt 14053 (Figure 5). A range in Al_2O_3/CaO is also observed in primitive pyroclastic glasses where Apollo 14 and 17 very low-Ti (VLT) glasses have higher Al contents than the majority of the green glasses (Al_2O_3/CaO up to 1.1; Delano, 1986). The lack of correlation between $\delta^{44/40}$Ca and Al content of the low-Ti basalts seems to preclude significant assimilation of isotopically light crustal anorthosite, which is a common hypothesis for the origin of the high-Al samples (e.g., Ringwood and Kesson, 1976).

An alternative explanation that is more in line with the Ca isotope evidence is that the pressure dependence of Al partitioning in orthopyroxene is responsible for the range in Al_2O_3/CaO. Partial melting of the same hybrid source at pressures lower than 2.0 GPa produces melts with higher Al content and Al_2O_3/CaO but identical $\delta^{44/40}$Ca (supplementary Figure S6). The multiple saturation depths of high-Al Apollo 14 and 17 glasses, however, are 1.8-1.9 GPa (Chen et al., 1982) and thus identical to that of the other green glasses. Alternatively, overturn of the lunar cumulate pile can have brought harzburgite cumulates that crystallised at higher pressure, and thus host Al-rich orthopyroxene, to shallower depths. Interaction of ascending low-Ti melts with such cumulates, as

proposed by e.g., Elkins-Tanton et al. (2003) and Barr and Grove (2013), is another possible process that could increase Al_2O_3/CaO of the melt, although re-equilibration with shallower cumulates might affect $\delta^{44/40}$Ca as well.

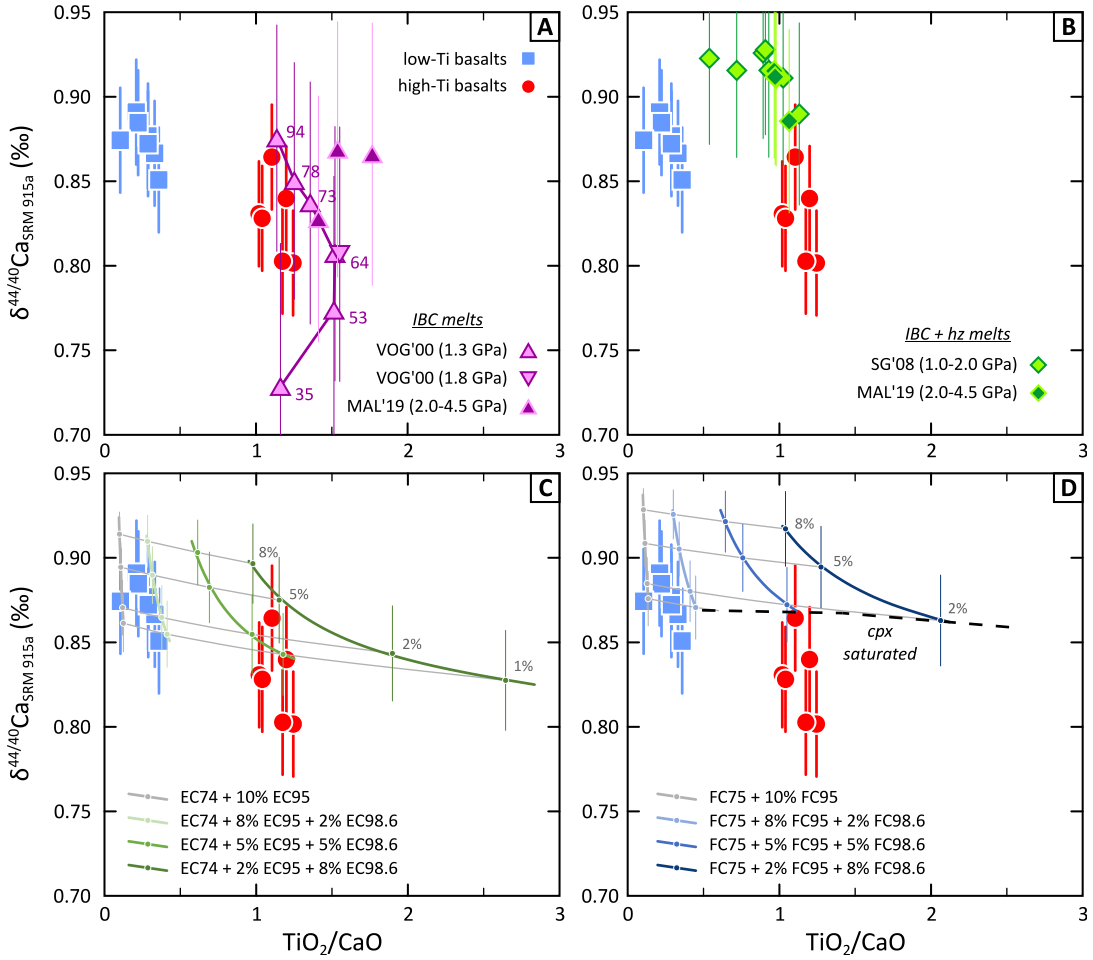

Figure 7. *Ca isotope composition constraints on the petrogenesis of lunar high-Ti magmas from TiO_2/CaO versus $\delta^{44/40}$Ca systematics. (a) Composition of the lunar samples in comparison to partial melts of ilmenite-bearing cumulates (IBC; EC98.6). The major element composition of the IBC melts is from the experimental studies of van Orman and Grove (2000) and Mallik et al. (2019) while $\delta^{44/40}$Ca is calculated from mass balance. Labels for the van Orman and Grove (2000) 1.3 GPa data are the percentage of melt. (b) Composition of the lunar samples in comparison to clinopyroxene-undersaturated partial melts of a hybrid source consisting of bulk IBC (EC98.6) and a harzburgite cumulate in a 1:1 proportion, based on the experimental studies of Singletary and Grove (2008) and Mallik et al. (2019). The Ca isotope composition of the partial melts is calculated from mass balance assuming that the harzburgite cumulate has $\delta^{44/40}$Ca = 1.150 ± 0.025‰ (Figure 2). (c) Modelled composition (pMELTS) of 1-8% batch melts (grey lines and labels) of a hybrid cumulate source consisting of EC74 harzburgite cumulates mixed with variable proportion of late-stage clinopyroxenite cumulates (EC95) and IBC (EC98.6). (d) same as panel C but for the FC model. The black dashed line indicates where partial melts become saturated in high-Ca pyroxene. Error bars ($\delta^{44/40}$Ca) for the melting model incorporate the uncertainty on the bulk Moon composition and the diopside-melt Ca isotope fractionation factor; see text and supplementary material for details.*

4.3. Constraints on the source composition of lunar high-Ti magmas

Ilmenite is the last phase to appear on the solidus of the residual melt after ca. 95–98% LMO solidification (e.g., Snyder et al., 1992; Charlier et al., 2018). The most evolved, ilmenite-bearing cumulates (IBC) are widely believed to play an important part in the petrogenesis of the lunar high-Ti magmas yet their exact role remains unclear (e.g., Ringwood and Kesson, 1976; Hess and Parmentier, 1995; Shearer et al., 2006; Krawczynski and Grove, 2012). Several experimental studies have investigated the melting relationships of IBC and bulk mixtures of IBC

and harzburgite cumulates (van Orman and Grove, 2000; Singletary and Grove, 2008; Thacker et al., 2009; Mallik et al., 2019), which can serve as a basis for exploring the Ca isotope constraints on high-Ti magma sources.

The mare basalts display a negative correlation between TiO_2/CaO and $\delta^{44/40}$Ca where the high-Ti basalts have on average lower $\delta^{44/40}$Ca (Figure 7). This observation suggests that simply adding ilmenite to a low-Ti source will not generate high-Ti magmas. Ilmenite is essentially Ca-free and has no leverage to modify Ca isotope compositions; hence an appropriate Ti-rich component needs to have low $\delta^{44/40}$Ca and a non-negligible Ca content. The IBC appear to match this criterion as they contain ca. 75% high-Ca pyroxene by weight (Figure 2). Partial melts of IBC have a TiO_2/CaO and $\delta^{44/40}$Ca signature that overlaps with the high-Ti basalts (Figure 7a) but are a poor match for other major elements (van Orman and Grove, 2000; Mallik et al., 2019). Moreover, high-degree IBC melts are saturated only in pigeonite whereas high-Ti melts are multiply saturated in olivine and orthopyroxene, as are low-Ti magmas (e.g., Longhi, 1992; Krawczynski and Grove, 2012). Major element systematics also effectively rule out binary mixing between low-Ti and IBC melts to produce the lunar high-Ti melts (Figure 8; van Orman and Grove, 2000). Hybrid sources consisting of IBC and harzburgite cumulates produce melts that do not have the right major element composition and $\delta^{44/40}$Ca to either reproduce the high-Ti magmas directly or to form a suitable mixing component with low-Ti magmas (Figures 7b and 8; Singletary and Grove, 2008; Mallik et al., 2019).

We investigate the composition of partial melts of IBC-bearing, tribrid sources using pMELTS. These sources consist of variable proportions of (i) harzburgite cumulates, (ii) late-stage clinopyroxenite cumulates (which together can produce the low-Ti magmas), and (iii) ilmenite-bearing cumulates. Partial melts of such tribrid sources have elevated TiO_2/CaO compared to low-Ti magmas but fail to reproduce the lower $\delta^{44/40}$Ca observed in the high-Ti basalts (Figure 7c-d). The addition of IBC to hybrid sources that already hybridised with a significant proportion of clinopyroxenite cumulates quickly causes clinopyroxene-saturation of the partial melts. In addition, Al_2O_3/CaO of the melts decreases markedly if IBC are added to the source. While primitive pyroclastic glasses do display a slight negative correlation between TiO_2/CaO and Al_2O_3/CaO, experimental studies on hybrid sources and the pMELTS models display a much more pronounced decrease in Al_2O_3/CaO than borne out by lunar samples (Figure 8). Hence, there appears to be a paradox; high-Ti basalts have lower $\delta^{44/40}$Ca than low-Ti basalts, but adding a Ca-rich, low-$\delta^{44/40}$Ca component to a low-Ti source increases the Ca content of that source too much, leading to clinopyroxene-saturation and too low Al_2O_3/CaO in partial melts of such tribrid sources.

A way around this limitation is a process in which $\delta^{44/40}$Ca of the high-Ti source decreases, the Ti content increases but the Ca content does not significantly increase. This seems possible when low-Ti hybrid sources are metasomatised by IBC melts. The solidus temperature of IBC is >100 °C lower than that of the harzburgite cumulates (van Orman and Grove, 2000) and, as such, downward transport of IBC during overturn of the cumulate pile will induce melting of the IBC (e.g., Ringwood and Kesson, 1976). These melts are likely to be positively buoyant (Mallik et al., 2019) and will infiltrate and react with the surrounding cumulates. Orthopyroxene in these cumulates is strongly Ti-undersaturated and thus has the potential to incorporate Ti from the IBC melt (e.g., Ringwood and Kesson, 1976; Shearer et al., 2006) to form an appropriate source for the high-Ti magmas. Experimental work suggests that ilmenite-saturated orthopyroxene can contain up to 1.5 wt.% TiO_2 (Thacker et al., 2009), compared to TiO_2 contents of <0.1 wt.% in orthopyroxene in green glass residua (Elkins-Tanton et al., 2003; Barr and Grove, 2013). On the other hand, orthopyroxene in the hybrid low-Ti sources is already close to Ca-saturation and might thus isotopically equilibrate Ca with the IBC melt, causing a decrease in $\delta^{44/40}$Ca in the hybrid cumulate, but this does not need to be accompanied by a significant increase in orthopyroxene Ca content or the precipitation of clinopyroxene.

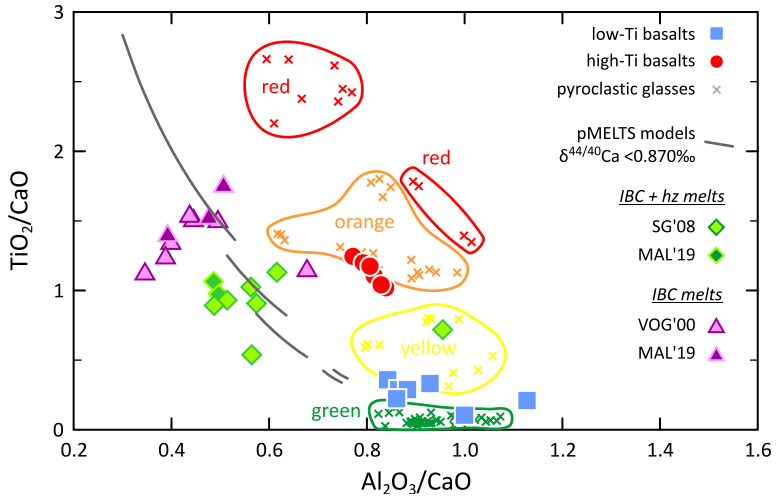

Figure 8. *Al_2O_3/CaO versus TiO_2/CaO diagram showing the mare basalts measured for $\delta^{44/40}$Ca in this study and primitive pyroclastic glasses (Delano, 1986; Shearer and Papike, 1993) in comparison with the composition of partial melts of ilmenite-bearing cumulates (IBC) and hybrid mantle sources found by experimental studies (van Orman and Grove, 2000; Singletary and Grove, 2008; Mallik et al., 2019) and pMELTS models. The pMELTS models are those shown in Figure 7c and d where melt compositions have $\delta^{44/40}$Ca <0.87‰. The composition of the mare basalts is corrected for low-pressure fractional crystallisation (see supplementary Figure S6).*

5. Conclusions

New Ca isotope data for lunar mare basalts indicate that low-Ti magmas can be produced by remelting of evolved harzburgite cumulates that have incorporated 8–15 wt.% of late-stage clinopyroxenite cumulates. Physical mixing of these cumulate reservoirs is likely achieved through gravitational overturn of the cumulate pile driven by the density contrast of deep harzburgite cumulates and shallow clinopyroxene±ilmenite cumulates (e.g., Hess and Parmentier, 1995). Our modelling shows that only remelting of such a hybrid source can adequately account for the $\delta^{44/40}$Ca composition of the low-Ti mare basalts whilst satisfying the constraints set by experimentally deduced high-pressure phase relations of these samples. The main implications of these results are:

(i) Late-stage clinopyroxene-rich, but ilmenite-free, cumulates play a crucial role in the petrogenesis of low-Ti magmas. Without the addition of a late-stage cumulate component, harzburgite cumulates alone are too Ca-poor to be able to generate melts with $\delta^{44/40}$Ca like the low-Ti basalts.

(ii) Refractory, trace element- and Ca-poor dunites and harzburgites precipitating during the first 75% of LMO solidification do not appear to be involved in mare magmatism.

(iii) For an LPUM bulk Moon composition, major element systematics indicate that the transition from equilibrium to fractional crystallisation occurred before or around 50% LMO solidification.

(iv) The similar $\delta^{44/40}$Ca of lunar basalts and terrestrial MORB is coincidental but fully consistent with a bulk Moon that has identical $\delta^{44/40}$Ca to the bulk silicate Earth.

The high-Ti basalts have more variable and slightly lower $\delta^{44/40}$Ca than the low-Ti basalts. Melting of hybrid sources containing IBC does not reproduce the lower $\delta^{44/40}$Ca and produces melts with too low Al_2O_3/CaO. A more plausible process to generate the high-Ti sources is metasomatism of hybrid low-Ti sources by IBC melts.

Acknowledgements

We greatly appreciated the efforts of Chris Coath and Thermo-Fisher Scientific in developing Ca isotope measurements protocols on Proteus and keeping it in perfect working order. Edgar Steenstra is thanked for fruitful discussions and his comments on the manuscript. Dan Bevan kindly provided Figure S1. Reviews by Justin Simon and an anonymous reviewer were of great help improving the manuscript. Rajdeep Dasgupta is thanked for careful editorial handling. MK and TE acknowledge funding by STFC through grant no. ST/M007715/1. MA

acknowledges funding from STFC grants #ST/P000657/1 and #ST/T000228/1. Development of Proteus was funded by the ERC through advanced grant ISONEB 321209.

CRediT author statement

Martijn Klaver: conceptualization, investigation, writing – original draft; **Tu-Han Luu**: methodology, investigation, writing – review and editing; **Jamie Lewis**: methodology, investigation; **Maximiliaan Jansen**: investigation, writing – review and editing; **Mahesh Anand**: resources, writing – review and editing; **Johannes Schwieters**: methodology; **Tim Elliott**: conceptualization, funding acquisition, writing – review and editing.

References

Antonelli, M.A., Simon, J.I., 2020. Calcium isotopes in high-temperature terrestrial processes. Chem. Geol. 548, 119651.

Arevalo, R., McDonough, W.F., 2010. Chemical variations and regional diversity observed in MORB. Chem. Geol. 271, 70-85.

Barr, J.A., Grove, T.L., 2013. Experimental petrology of the Apollo 15 group A green glasses: Melting primordial lunar mantle and magma ocean cumulate assimilation. Geochim. Cosmochim. Acta 106, 216-230.

Bevan, D., Coath, C.D., Lewis, J., Schwieters, J., Lloyd, N., Craig, G., Wehrs, H., Elliott, T., 2021. In situ Rb–Sr dating by collision cell, multicollection inductively-coupled plasma mass-spectrometry with pre-cell mass-filter (CC-MC-ICPMS/MS). J. Anal. At. Spectrom.

Borg, L.E., Gaffney, A.M., Shearer, C.K., 2015. A review of lunar chronology revealing a preponderance of 4.34–4.37 Ga ages. Meteorit. Planet. Sci. 50, 715-732.

Charlier, B., Grove, T.L., Namur, O., Holtz, F., 2018. Crystallization of the lunar magma ocean and the primordial mantle-crust differentiation of the Moon. Geochim. Cosmochim. Acta 234, 50-69.

Chen, C., Ciazela, J., Li, W., Dai, W., Wang, Z., Foley, S.F., Li, M., Hu, Z., Liu, Y., 2020. Calcium isotopic compositions of oceanic crust at various spreading rates. Geochim. Cosmochim. Acta 278, 272-288.

Chen, C., Dai, W., Wang, Z., Liu, Y., Li, M., Becker, H., Foley, S.F., 2019. Calcium isotope fractionation during magmatic processes in the upper mantle. Geochim. Cosmochim. Acta 249, 121-137.

Chen, H.K., Delano, J., Lindsley, D., 1982. Chemistry and phase relations of VLT volcanic glasses from Apollo 14 and Apollo 17. Journal of Geophysical Research: Solid Earth 87, A171-A181.

Delano, J.W., 1986. Pristine lunar glasses: Criteria, data, and implications. Journal of Geophysical Research: Solid Earth 91, 201-213.

Elardo, S.M., Draper, D.S., Shearer Jr, C.K., 2011. Lunar Magma Ocean crystallization revisited: Bulk composition, early cumulate mineralogy, and the source regions of the highlands Mg-suite. Geochim. Cosmochim. Acta 75, 3024-3045.

Elkins-Tanton, L.T., Burgess, S., Yin, Q.-Z., 2011. The lunar magma ocean: Reconciling the solidification process with lunar petrology and geochronology. Earth Planet. Sci. Lett. 304, 326-336.

Elkins-Tanton, L.T., Chatterjee, N., Grove, T.L., 2003. Experimental and petrological constraints on lunar differentiation from the Apollo 15 green picritic glasses. Meteorit. Planet. Sci. 38, 515-527.

Ghiorso, M.S., Hirschmann, M.M., Reiners, P.W., Kress III, V.C., 2002. The pMELTS: A revision of MELTS for improved calculation of phase relations and major element partitioning related to partial melting of the mantle to 3 GPa. Geochem. Geophys. Geosyst. 3, 1-35.

Giguere, T.A., Taylor, G.J., Hawke, B.R., Lucey, P.G., 2000. The titanium contents of lunar mare basalts. Meteorit. Planet. Sci. 35, 193-200.

Hallis, L., Anand, M., Strekopytov, S., 2014. Trace-element modelling of mare basalt parental melts: implications for a heterogeneous lunar mantle. Geochim. Cosmochim. Acta 134, 289-316.

Hess, P.C., 2000. On the source regions for mare picrite glasses. Journal of Geophysical Research: Planets 105, 4347-4360.

Hess, P.C., Parmentier, E., 1995. A model for the thermal and chemical evolution of the Moon's interior: Implications for the onset of mare volcanism. Earth Planet. Sci. Lett. 134, 501-514.

Huang, F., Zhou, C., Wang, W., Kang, J., Wu, Z., 2019. First-principles calculations of equilibrium Ca isotope fractionation: Implications for oldhamite formation and evolution of lunar magma ocean. Earth Planet. Sci. Lett. 510, 153-160.

Huang, S., Farkaš, J., Jacobsen, S.B., 2011. Stable calcium isotopic compositions of Hawaiian shield lavas: evidence for recycling of ancient marine carbonates into the mantle. Geochim. Cosmochim. Acta 75, 4987-4997.

Huang, S., Jacobsen, S.B., 2017. Calcium isotopic compositions of chondrites. Geochim. Cosmochim. Acta 201, 364-376.

Hughes, S., Delano, J., Schmitt, R., 1988. Apollo 15 yellow-brown volcanic glass: Chemistry and petrogenetic relations to green volcanic glass and olivine-normative mare basalts. Geochim. Cosmochim. Acta 52, 2379-2391.

Jacobson, A.D., Andrews, M.G., Lehn, G.O., Holmden, C., 2015. Silicate versus carbonate weathering in Iceland: New insights from Ca isotopes. Earth Planet. Sci. Lett. 416, 132-142.

Kang, J.-T., Ionov, D.A., Liu, F., Zhang, C.-L., Golovin, A.V., Qin, L.-P., Zhang, Z.-F., Huang, F., 2017. Calcium isotopic fractionation in mantle peridotites by melting and metasomatism and Ca isotope composition of the Bulk Silicate Earth. Earth Planet. Sci. Lett. 474, 128-137.

Kommescher, S., Fonseca, R., Kurzweil, F., Thiemens, M., Münker, C., Sprung, P., 2020. Unravelling lunar mantle source processes via the Ti isotope composition of lunar basalts. Geochemical Perspectives Letters 13, 13-18.

Krawczynski, M.J., Grove, T.L., 2012. Experimental investigation of the influence of oxygen fugacity on the source depths for high titanium lunar ultramafic magmas. Geochim. Cosmochim. Acta 79, 1-19.

Lin, Y., Tronche, E.J., Steenstra, E.S., van Westrenen, W., 2017. Evidence for an early wet Moon from experimental crystallization of the lunar magma ocean. Nat. Geosci. 10, 14-18.

Lock, S.J., Stewart, S.T., Petaev, M.I., Leinhardt, Z., Mace, M.T., Jacobsen, S.B., Cuk, M., 2018. The origin of the Moon within a terrestrial synestia. Journal of Geophysical Research: Planets 123, 910-951.

Longhi, J., 1992. Experimental petrology and petrogenesis of mare volcanics. Geochim. Cosmochim. Acta 56, 2235-2251.

Longhi, J., 2006. Petrogenesis of picritic mare magmas: constraints on the extent of early lunar differentiation. Geochim. Cosmochim. Acta 70, 5919-5934.

Mallik, A., Ejaz, T., Shcheka, S., Garapic, G., 2019. A petrologic study on the effect of mantle overturn: Implications for evolution of the lunar interior. Geochim. Cosmochim. Acta 250, 238-250.

Rapp, J., Draper, D., 2018. Fractional crystallization of the lunar magma ocean: Updating the dominant paradigm. Meteorit. Planet. Sci. 53, 1432-1455.

Ringwood, A., Kesson, S., 1976. A dynamic model for mare basalt petrogenesis, Lunar and Planetary Science Conference Proceedings, pp. 1697-1722.

Schiller, M., Bizzarro, M., Fernandes, V.A., 2018. Isotopic evolution of the protoplanetary disk and the building blocks of Earth and the Moon. Nature 555, 507-510.

Shearer, C., Papike, J., 1993. Basaltic magmatism on the Moon: A perspective from volcanic picritic glass beads. Geochim. Cosmochim. Acta 57, 4785-4812.

Shearer, C.K., Hess, P.C., Wieczorek, M.A., Pritchard, M.E., Parmentier, E.M., Borg, L.E., Longhi, J., Elkins-Tanton, L.T., Neal, C.R., Antonenko, I., 2006. Thermal and magmatic evolution of the Moon. Rev. Mineral. Geochem. 60, 365-518.

Simon, J., Jordan, M., Tappa, M., Schauble, E., Kohl, I., Young, E., 2017. Calcium and titanium isotope fractionation in refractory inclusions: Tracers of condensation and inheritance in the early solar protoplanetary disk. Earth Planet. Sci. Lett. 472, 277-288.

Simon, J.I., DePaolo, D.J., 2010. Stable calcium isotopic composition of meteorites and rocky planets. Earth Planet. Sci. Lett. 289, 457-466.

Singletary, S., Grove, T., 2008. Origin of lunar high-titanium ultramafic glasses: A hybridized source? Earth Planet. Sci. Lett. 268, 182-189.

Smith, J.V., Anderson, A.T., Newton, R.C., Olsen, E.J., Crewe, A.V., Isaacson, M.S., Johnson, D., Wyllie, P.J., 1970. Petrologic history of the moon inferred from petrography, mineralogy and petrogenesis of Apollo 11 rocks, Proceedings of the Apollo 11 Lunar Science Conference, pp. 897-926.

Snape, J.F., Nemchin, A.A., Bellucci, J.J., Whitehouse, M.J., Tartèse, R., Barnes, J.J., Anand, M., Crawford, I.A., Joy, K.H., 2016. Lunar basalt chronology, mantle differentiation and implications for determining the age of the Moon. Earth Planet. Sci. Lett. 451, 149-158.

Snyder, G.A., Taylor, L.A., Neal, C.R., 1992. A chemical model for generating the sources of mare basalts: Combined equilibrium and fractional crystallization of the lunar magmasphere. Geochim. Cosmochim. Acta 56, 3809-3823.

Sossi, P.A., Moynier, F., 2017. Chemical and isotopic kinship of iron in the Earth and Moon deduced from the lunar Mg-Suite. Earth Planet. Sci. Lett. 471, 125-135.

Steenstra, E., Berndt, J., Klemme, S., Fei, Y., van Westrenen, W., 2020. A possible high-temperature origin of the Moon and its geochemical consequences. Earth Planet. Sci. Lett. 538, 116222.

Suckale, J., Elkins-Tanton, L.T., Sethian, J.A., 2012. Crystals stirred up: 2. Numerical insights into the formation of the earliest crust on the Moon. Journal of Geophysical Research: Planets 117.

Thacker, C., Liang, Y., Peng, Q., Hess, P., 2009. The stability and major element partitioning of ilmenite and armalcolite during lunar cumulate mantle overturn. Geochim. Cosmochim. Acta 73, 820-836.

Thiemens, M.M., Sprung, P., Fonseca, R.O., Leitzke, F.P., Münker, C., 2019. Early Moon formation inferred from hafnium–tungsten systematics. Nat. Geosci. 12, 696-700.

Valdes, M.C., Moreira, M., Foriel, J., Moynier, F., 2014. The nature of Earth's building blocks as revealed by calcium isotopes. Earth Planet. Sci. Lett. 394, 135-145.

van Orman, J.A., Grove, T.L., 2000. Origin of lunar high-titanium ultramafic glasses: Constraints from phase relations and dissolution kinetics of clinopyroxene-ilmenite cumulates. Meteorit. Planet. Sci. 35, 783-794.

Warren, P.H., 1985. The magma ocean concept and lunar evolution. Annual Review of Earth and Planetary Sciences 13, 201-240.

Wood, J.A., Dickey Jr, J.S., Marvin, U.B., Powell, B.N., 1970. Lunar anorthosites and a geophysical model of the moon, Proceedings of the Apollo 11 Lunar Science Conference, pp. 965-988.

Wu, W., Xu, Y.-G., Zhang, Z.-F., Li, X., 2020. Calcium isotopic composition of the lunar crust, mantle, and bulk silicate Moon: A preliminary study. Geochim. Cosmochim. Acta 270, 313-324.

Zhang, H., Wang, Y., He, Y., Teng, F.Z., Jacobsen, S.B., Helz, R.T., Marsh, B.D., Huang, S., 2018. No measurable calcium isotopic fractionation during crystallization of Kilauea Iki lava lake. Geochem. Geophys. Geosyst. 19, 3128-3139.

Zhu, H., Liu, F., Li, X., Wang, G., Zhang, Z., Sun, W., 2018. Calcium isotopic compositions of normal Mid-Ocean Ridge basalts from the southern Juan de Fuca Ridge. Journal of Geophysical Research: Solid Earth 123, 1303-1313.

SUPPLEMENTARY MATERIAL

Contents:

Supplementary Datasets (Excel files; please email the corresponding author for these files)

1. Major element and Ca isotope composition of the studied samples corrected for the effects of low-pressure fractional crystallisation
2. LMO crystallisation models
3. pMELTS models

1. Extended analytical techniques

Full details of the analytical techniques used to measure Ca isotopes on the Proteus collision cell MC-ICP-MS/MS are provided in Lewis et al. (2021; in preparation as an invited manuscript for Chemical Geology). A summary containing all pertinent details is provided below.

1.1. Preparation of the samples

Calcium isotope composition measurements were performed on aliquots of homogeneous powders (ca. 250 mg material) previously characterised for their major- and trace element composition by Hallis et al. (2014). For this study, the aliquots were digested in concentrated HF/HNO_3 (3:1) for four days. The digestion residua were treated with concentrated HNO_3 twice and taken up in 2.0 M HNO_3 prior to further processing. Samples were measured for both their mass-dependent deviation from reference material NIST SRM 915a (reported as $\delta^{44/40}Ca_{SRM\ 915a}$; hereafter abbreviated to $\delta^{44/40}Ca$) using a double spike technique, and for radiogenic anomalies on ^{40}Ca, produced by the decay of ^{40}K, through internal normalisation to $^{42}Ca/^{44}Ca$ to correct for all mass-dependent isotope fractionation (reported as $\Delta'_{42/44}{}^{40/44}Ca_{SRM\ 915a}$; hereafter abbreviated to $\Delta'^{40/44}Ca$). For $\delta^{44/40}Ca$ measurements, an aliquot of the digested sample was equilibrated with a ^{42}Ca–^{43}Ca double spike, taking care to match the sample-spike proportion to within 5% of spiked reference material SRM 915a that was used as bracketing calibrator.

The preparation of the samples for radiogenic and mass-dependent measurements used different sets of columns and other non-disposable labware to prevent cross-contamination, but otherwise identical procedures were followed. Separation of Ca from the matrix followed a three-step purification procedure. The first column separation used 1 mL of AG50W-X12 cation exchange resin in a 2 mL BioRad column. After loading the sample solution in 0.4 M HCl, 0.5 M HF was used to elute Al, Ti and Fe. Alkalis and Cr were subsequently eluted with 0.4M HCl, Mg with 1 M HCl and finally the Ca–Sr fraction was collected with 6 M HCl. In order to minimise the isobaric interference of doubly-charged Sr, the Ca fraction was further purified on a high-aspect ratio quartz glass column filled with 2.5 mL AG50W-X12 resin where Ca was mostly separated from Sr with 2.5 M HCl. A final clean-up step involved a small pipette tip column with ca. 0.1 mL Sr specific resin (Horwitz et al., 1992) where Ca was eluted in 3.0 M HNO_3 whereas any remaining Sr was retained on the resin, to be subsequently eluted with water. The purified Ca fractions were treated with concentrated HNO_3 twice to remove any leftover organic material (e.g., from the resin) and subsequently dissolved in 0.3 M HNO_3 to obtain ca. 5 µg/mL Ca solutions for measurement on Proteus.

1.2. Ca isotope measurements with Proteus

The main analytical advancement of our method is the use of a unique, tribrid MC-ICP-MS instrument dubbed Proteus (CC-MC-ICP-MS/MS), which was developed in collaboration between Thermo Fisher Scientific (Bremen) and the University of Bristol (see Bevan et al., 2021). In brief, Proteus combines a low-energy front end largely derived from the Thermo Fisher Scientific iCAP Q instrument consisting of a quadrapole mass pre-filter followed by a collision cell (CC), with a conventional Neptune Plus analyser (Figure S1). The collision cell serves to react ions in the sample ion beam with reaction and collision gases, either to remove direct isobaric interferences (e.g., the near-quantitative elimination of Ar^+ through reaction with H_2 as used in this study; see Eiden et al., 1996) or to promote of the analyte of interest to an interference-free part of the mass spectrum (e.g., the reaction of Sr^+ ions with SF_6 to form SrF^+; see Hogmalm et al., 2017 and Bevan et al., 2021).

For Ca isotope measurements in this study, He and H_2 gases are used in the collision cell. Helium (2 mL/min) is used as a collision gas to reduce the thermal energy spread of the ions and improve ion transmission through the collision cell. Hydrogen (3.4 mL/min) gas effectively charge neutralises Ar^+ to Ar^0 without deterioration of Ca^+ ion beam transmission. Typically, the $^{40}Ar^+$ ion beam intensity was reduced to <0.01 pA compared to 0.7–1.3 nA $^{40}Ca^+$.

Proteus was operated in medium resolution mode ($m/\Delta m$ ≥5500; 5–95% peak height definition) and the mass dispersion of the instrument allows static measurement of the mass spectrum from ^{39}K (Faraday cup L3) to ^{44}Ca (Faraday cup H3; see Table S1). All ion beams were measured using amplifiers fitted with default 10^{11} Ω

resistors, with the exception of a 10^{10} Ω resistor used in the amplifier for the measurement of $^{40}Ca^{+}$ on Faraday cup L2 (Table 1). Isobaric interference of K and doubly-charged Sr ions was monitored on $^{39}K^{+}$ and $^{87}Sr^{++}$ (using the compact discrete dynode secondary electron multiplier attached to Faraday cup H2) and corrected for using the K and Sr isotope compositions reported by Steiger and Jäger (1977) and Nier (1938), respectively.

Calcium isotope composition measurements were conducted on purified Ca solutions with a concentration of ca. 5 µg/mL, which yielded total Ca ion beam intensities (sample + double spike) between 1.25 and 1.50 nA. Purified samples yielded $^{39}K^{+}$ ion beam intensities of ca. 0.3 pA and <200 counts per second $^{87}Sr^{++}$. Care was taken to match sample ion beam intensity and, for mass-dependent measurements, sample–spike proportion to those of (spiked) NIST SRM 915a, which was used as bracketing calibrator. A sample measurement consisted of 30 cycles of 8.4 s integration time, preceded by an instrumental blank measurement (aspirating 0.3 M HNO_3) and bracketed by a measurement of (spiked) SRM 915a. The total amount of Ca consumed per measurement was ca. 1.5 µg. Each sample was measured at least six times (but for some samples up to 20 times; see Table 1 in the main text) in different analytical sessions. Data were processed offline. After correcting for blank contribution and isobaric interference, radiogenic $\Delta'^{40/44}Ca_{SRM\ 915a}$ data were corrected for exponential-law mass-dependent fractionation (natural plus analytical) through internal normalisation to $^{42}Ca/^{44}Ca = 0.31221$ (Russell et al., 1978). Inversion of the double spike equations to yield $\delta^{44/40}Ca$ relative to the two adjacent measurements of spiked SRM 915a followed the numerical approach presented by Rudge et al. (2009).

Table S1. *Cup configuration used for Ca isotope measurements on Proteus.*

Cup	**L3**	**L2**	**L1**	**C**	**H1**	**H2**	**H3**
Resistor	10^{11} Ω	10^{10} Ω	10^{11} Ω	10^{11} Ω	10^{11} Ω	SEM	10^{11} Ω
Isotope	$^{39}K^{+}$	$^{40}Ca^{+}$	$^{41}K^{+}$	$^{42}Ca^{+}$	$^{43}Ca^{+}$	$^{87}Sr^{++}$	$^{44}Ca^{+}$

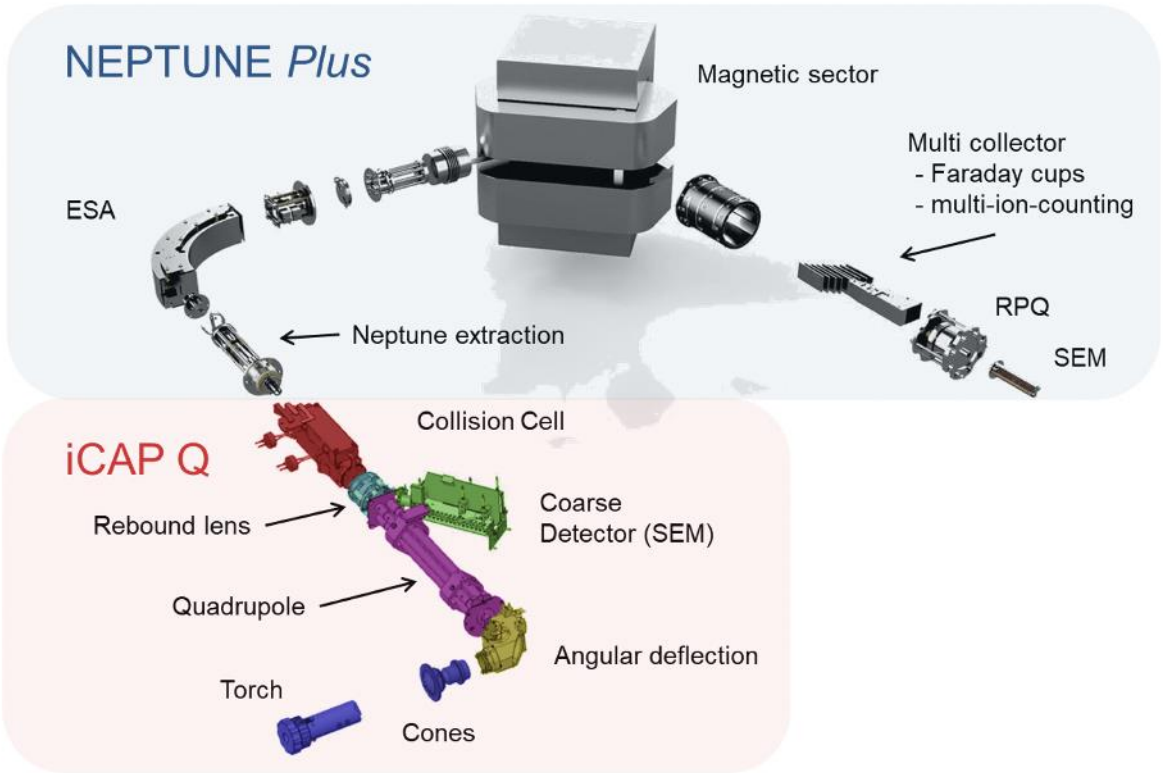

Figure S1. *Schematic diagram of the CC-MC-ICP-MS/MS instrument Proteus at the Bristol Isotope Group (Bevan et al., 2021).*

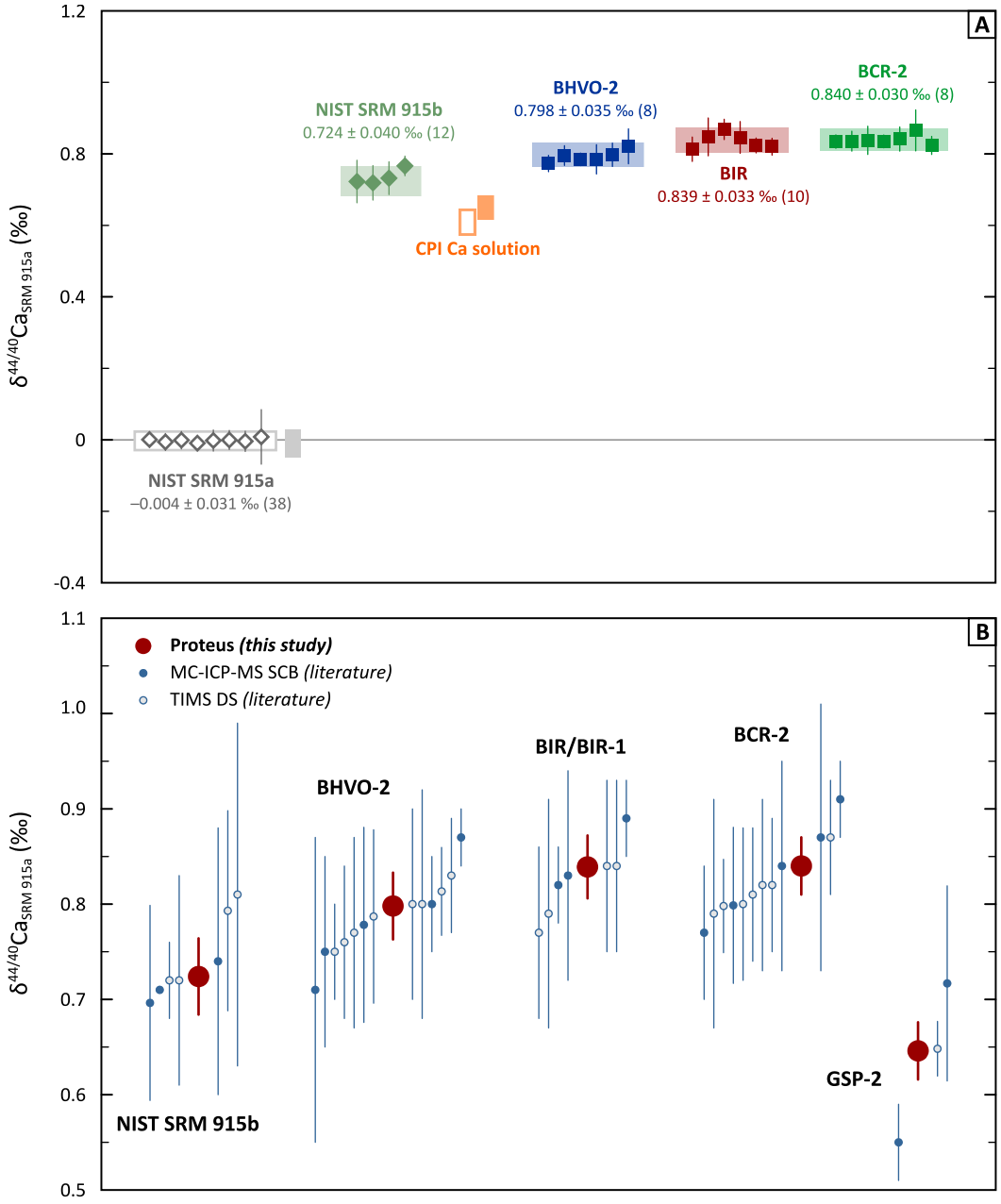

Figure S2. *Reference material $\delta^{44/40}$Ca data. A) Measurements of synthetic Ca (SRM 915a, SRM 915b, CPI Ca solution), geostandards (BHVO-2, BCR-2) and in-house BIR rock powder (Icelandic basalt taken from the same outcrop as USGS geostandard BIR-1) made alongside the lunar samples in this study (symbols) compared to data obtained over a ca. one-year period (boxes; Lewis et al., 2021). Filled symbols/boxes are for geostandards and synthetic Ca reference materials processed through the Ca purification procedure, open symbols/boxes for unprocessed Ca solutions. Error bars are 2s measurement precision; the quoted uncertainty on the average is the 2s intermediate precision for all data for each reference material (Lewis et al., 2021) with the total number of measurements given in brackets. The pooled 2s intermediate precision for all reference materials (n = 84) is 0.034‰ (Lewis et al., 2021). B) Comparison of our results for reference materials to values published elsewhere (Heuser and Eisenhauer, 2008; Amini et al., 2009; Valdes et al., 2014; Amsellem et al., 2017; Feng et al., 2017; He et al., 2017; Kang et al., 2017; Simon et al., 2017; Zhang et al., 2018; Zhu et al., 2018; Chen et al., 2019; Chen et al., 2020; Wu et al., 2020; Zhu et al., 2020; Li and Han, 2021) showing the excellent agreement of the new Proteus data with conventional techniques (sample-calibrator bracketing [SCB] on MC-ICP-MS and double spike TIMS). Note that our GSP-2 $\delta^{44/40}$Ca data are corrected for its notable radiogenic ^{40}Ca anomaly (see Figure S3); literature values for GSP-2 are recalculated from reported $\delta^{44/42}$Ca data.*

1.3. Data quality

Mass-dependent ($\delta^{44/40}$Ca) and radiogenic ($\Delta'^{40/44}$Ca) data for reference materials (synthetic Ca solutions and geostandards) measured over the ca. one-year period of this study are shown Figures S2 and S3, respectively. Reference material measurements made directly alongside the lunar samples are shown as individual datapoints whereas the range of a larger pool of data obtained over a period of ca. one year (Lewis et al., 2021) is shown as boxes. We define a measurement as the average of typically four to eight repeats of the same purified Ca solution measured during a single analytical session (i.e., one day) where the error bar is the 2s precision of these repeats (repeatability conditions).

Typical 2s intermediate precision for a reference material (i.e., two times the standard deviation of measurements spanning a period of ca. one year, measured under similar conditions and, in case of geostandards, comprising multiple digestions and/or purified Ca fractions) is ca. 0.030–0.035‰ for $\delta^{44/40}$Ca (Figure S2) and 0.04-0.05‰ for $\Delta'^{40/44}$Ca (Figure S3). The pooled (homoscedastic) 2s intermediate precision of all measurements of reference materials shown in Figures S2 and S3 (see also Lewis et al., 2021), is 0.034‰ for $\delta^{44/40}$Ca (n = 84) and 0.049‰ for $\Delta'^{40/44}$Ca (n = 225), which we take as the best estimate for the uncertainty on our sample measurements.

Note that the $\delta^{44/40}$Ca results for the lunar samples that are presented in Table 1 in the main text include more repeats (up to 20) of a single purified Ca fraction obtained over two to four analytical sessions compared to the individual data points for reference materials shown in Figure S2. As a result, the uncertainty quoted in Table 1 in the main text (the two standard error precision obtained under repeatability conditions) is notably smaller than the pooled intermediate precision of the reference materials (0.034‰), but the latter serves as a more robust estimate of the uncertainty of our method.

The uncertainty on $\delta^{44/40}$Ca data obtained with Proteus (0.034‰) represents a marked improvement over previous studies that typically report 2s intermediate precisions of ≥0.1‰. There are several reasons for the lower uncertainties of the Proteus data compared to traditional Ca isotope methods. As Ar^+ is nearly quantitatively eliminated, Proteus allows for direct measurement of the $^{40}Ca^+$ ion beam. The excellent intermediate precision of our mass-independent data ($\Delta'^{40/44}$Ca) for reference materials (Figure S3) illustrates that Proteus can reliably be used for the measurement of $^{40}Ca^+$. As a result, we can use a ^{42}Ca–^{43}Ca double spike with ^{40}Ca and ^{44}Ca as additional inversion isotopes, which allows the measurement of the most abundant Ca isotopes in a setup with minimum mass dispersion around the axial Faraday detector (Holmden, 2005).

Compared to double spike TIMS methods, MC-ICP-MS instruments generally offer better reproducibility as they allow for rapid sample-calibrator bracketing with spiked reference materials to be used as a secondary correction for any non-exponential law fractionation effects that are not covered by the double spike approach. For instance, in MC-ICP-MS measurement sessions, the ion beam focussing is constant, which means that static MC-ICP-MS measurements suffer less from variable cup efficiency factors than TIMS measurements where sample loading on filaments causes differences in ion beam geometry on a sample-to-sample basis (e.g., Caro et al., 2010; Holmden and Bélanger, 2010). In addition, due to the higher beam intensities readily achieved by MC-ICP-MS, the total integration time for a sample measurement can be greatly reduced to obtain the same counting statistics as for TIMS (cf., DePaolo, 2004), and as a result the time between bracketed reference material measurements can be short (e.g., Albarède and Beard, 2004).

Previous studies that performed Ca isotope measurements by MC-ICP-MS (see Figure 2b), however, could not take advantage of some of the benefits described above as direct measurement of $^{40}Ca^+$ was outside their reach. Most MC-ICP-MS studies did not use a double spike approach and relied solely on sample-calibrator bracketing to correct for instrumental mass fractionation. This measurement strategy is suboptimal as matrix effects may cause differential mass fractionation between samples and the calibrator, thus introducing a bias in sample data that is difficult to recognise on a sample-by-sample basis (e.g., Klaver and Coath, 2019). There is also the risk of effects from potential non-quantitative yields during the Ca purification procedure. By employing the double spike method to correct for instrumental mass fractionation and subsequently bracketing the measurements of unknowns with spiked reference material SRM 915a, we were able to improve the uncertainty of our measurements (Figure S2).

To summarise, measuring Ca isotope ratios using Proteus combines the best of both worlds; the small mass dispersion setup where $^{40}Ca^{+}$ can be directly measured normally reserved to TIMS, and the advantage of rapid bracketing with spiked reference materials enabled by MC-ICP-MS.

We have performed several checks to substantiate the robustness of our new data. First, aliquots of several pure Ca reference materials (NIST SRM 915a and our in-house ICP Ca solution) that were processed through the ion-exchange Ca isolation procedure (section 1.1) yield results that are indistinguishable from aliquots that did not undergo purification for both $\delta^{44/40}Ca$ and $\Delta'^{40/44}Ca$ (Figures S2 and S3). This indicates that no artefacts are introduced during the ion-exchange procedure that are not corrected for by the double spike. In addition, it illustrates that Ca procedural blanks are negligible compared to the amount of Ca processed for the measurements. Second, our results for geostandards and NIST SRM 915b are in excellent agreement with published values (Figure S2B), which implies that Ca isotope data obtained with Proteus are directly comparable to literature data (e.g., the BSE value as derived from published data for fertile peridotites).

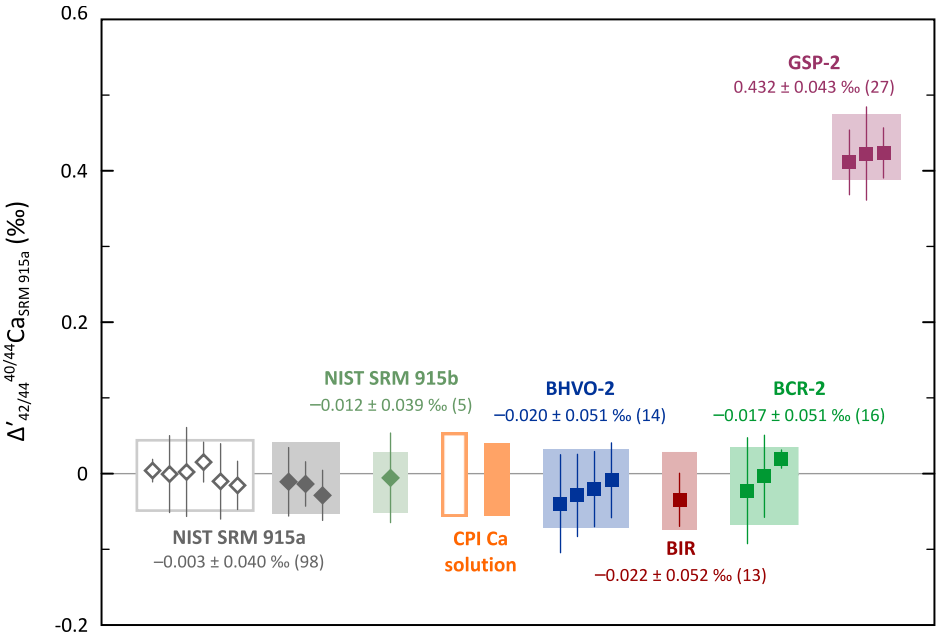

Figure S3. *Radiogenic $\Delta'^{40/44}Ca$ results for reference materials. Symbols are measurements made directly alongside the lunar samples; the boxes include all data measured over a ca. one-year period (Lewis et al., 2021). Filled symbols/boxes are for geostandards and synthetic Ca reference materials processed through the Ca purification procedure, open symbols/boxes for unprocessed Ca solutions. Error bars are 2s measurement precision; the quoted uncertainty on the average is the 2s intermediate precision for all data with the number of measurements given in brackets (Lewis et al., 2021). The pooled 2s intermediate precision for all reference materials (n = 225) is 0.049‰ (Lewis et al. 2021).*

2. Radiogenic ^{40}Ca results

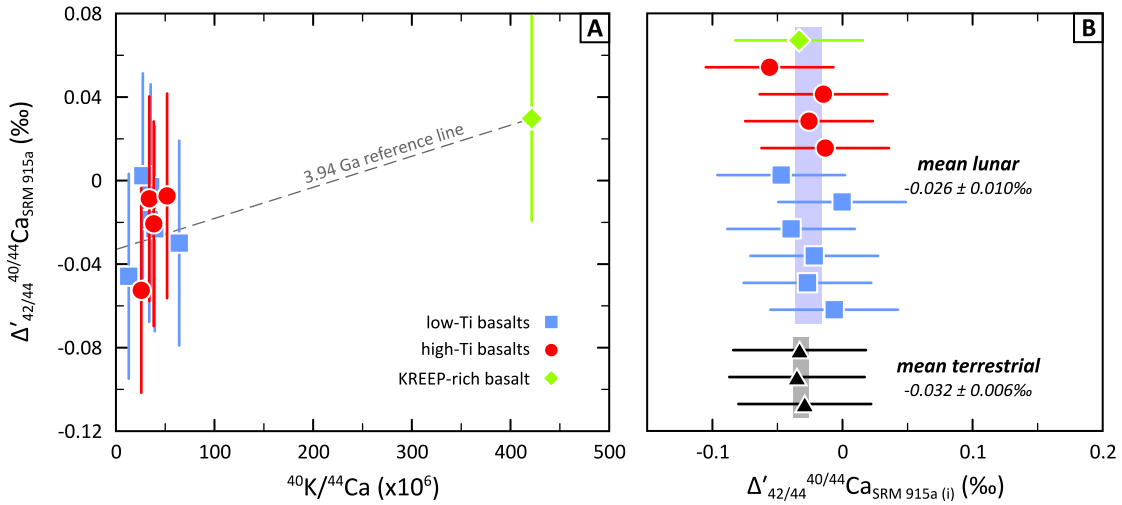

Figure S4. *Radiogenic ^{40}Ca isotope composition ($\Delta'_{42/44}{}^{40/44}Ca_{SRM\ 915a}$) of the lunar samples. A) Isochron-type diagram versus $^{40}K/^{44}Ca$ of the lunar basalts. The reference line through the KREEP-rich basalt is for its 3.94 Ga eruption age to show the effect of radiogenic ingrowth. B) Initial $\Delta'_{42/44}{}^{40/44}Ca$ corrected for radiogenic ingrowth to the eruption age of the sample (Table S2) is homogeneous at -0.026 ± 0.010‰ (2s). The terrestrial initial $\Delta'_{42/44}{}^{40/44}Ca$ (-0.032 ± 0.006‰; 2s) is estimated from the measured composition of three terrestrial basalts measured over the course of this study, corrected for 4.56 Ga of radiogenic ingrowth at $^{40}K/^{44}Ca$ of the primitive mantle (Palme and O'Neill, 2014); see Table S1.*

Table S2. *Radiogenic Ca isotope composition of the lunar samples and terrestrial basalts relative to SRM 915a.*

sample	suite	$\Delta'^{40/44}Ca$ ‰	CaO* (wt.%)	K_2O* (wt.%)	Age† Ga	$^{40}K/^{44}Ca$ ×10^6	$\Delta'^{40/44}Ca_{(i)}$‰	2s‡
10020	high-Ti	-0.009	11.25	0.056	3.77	33.8	-0.013	0.049
10050	high-Ti	-0.021	12.14	0.069	3.75	38.4	-0.026	0.049
74275	high-Ti	-0.007	10.58	0.081	3.85	51.9	-0.015	0.049
75055	high-Ti	-0.053	11.85	0.045	3.78	25.7	-0.056	0.049
15386	KREEP-rich	0.030	10.22	0.636	3.94	421.5	-0.033	0.049
12040	low-Ti	-0.003	8.03	0.042	3.30	35.3	-0.006	0.049
12052	low-Ti	-0.023	11.33	0.066	3.28	39.5	-0.027	0.049
12064	low-Ti	-0.019	12.55	0.063	3.18	33.8	-0.022	0.049
14053	low-Ti	-0.030	12.24	0.116	3.94	64.2	-0.040	0.049
15016	low-Ti	0.002	9.33	0.038	3.29	27.3	0.000	0.049
15555	low-Ti	-0.046	10.4	0.020	3.31	13.0	-0.047	0.049
Moon							**-0.026**	**0.010**
BHVO-2		-0.020	3.65	0.031	4.56	58.1	-0.033	0.051
BIR		-0.022	3.65	0.031	4.56	58.1	-0.035	0.052
BCR-2		-0.017	3.65	0.031	4.56	58.1	-0.029	0.051
Earth							**-0.032**	**0.003**

** Data from Hallis et al. (2014). For the terrestrial samples, CaO and K_2O are those of the primitive mantle (Palme and O'Neill, 2014).*

† Eruption age from the Lunar Sample Compendium https://curator.jsc.nasa.gov/lunar/lsc/index.cfm

‡ For the lunar samples, the 2s uncertainty is the intermediate precision for reference materials shown in Figure S1. For the terrestrial basalts that were measured multiple times, this is the 2s intermediate precision of the repeat measurements shown in Figure S3. No uncertainty on K/Ca or the age was propagated. Mean lunar and terrestrial are the 2 standard error of the mean.

$\Delta'^{40/44}Ca_{(i)}$ is corrected for radiogenic ingrowth since the eruption age using the decay constant of Steiger and Jäger (1977).

3. Comparison to published data for lunar basalts

Mass-dependent Ca isotope compositions ($\delta^{44/40}$Ca) of lunar basalts have previously been reported in several studies for Apollo samples (Simon and DePaolo, 2010; Valdes et al., 2014; Simon et al., 2017; Schiller et al., 2018) and lunar basaltic meteorites (Wu et al., 2020). A comparison of data from this study with published data is shown in Figure S5. In general, the agreement with previous studies is good and, for the low-Ti basalts, the average compositions of data in Valdes et al. (2014), Schiller et al. (2018) and Wu et al. (2020) overlap with our low-Ti basalt average (0.87 ± 0.03‰), although the range in values reported in these studies is larger and outside the quoted analytical uncertainties compared to our results. The latter is not necessarily surprising given that our method is likely more robust and precise compared to conventional methods (see section 1.3).

The Ca isotope compositions reported by Simon and DePaolo (2010) and Simon et al. (2017), however, are systematically heavier than the result from this study and other published data for both low- and high-Ti basalts (Figure S5). Notably, these authors report $\delta^{44/40}$Ca for two Apollo samples also included in our sample set where the results differ significantly; low-Ti basalt 15555 yields 0.87 ± 0.03‰ versus 1.02 ± 0.12‰ and high-Ti basalt 70215 yields 0.80 ± 0.03‰ versus 0.98 ± 0.12‰, for our data versus Simon et al. (2017), respectively. The reasons for this discrepancy are not fully understood. One possibility is heterogeneity of the mare basalts on a sample aliquot scale (10–500 mg), as for instance documented for Mg isotope compositions (Sedaghatpour and Jacobsen, 2019). Given that the discrepancy appears to be systematic rather than random, it seems more likely to arise from an inter-laboratory bias. The data in Simon and DePaolo (2010) and Simon et al. (2017) were obtained using a ^{43}Ca–^{48}Ca double spike and measured by TIMS. Their results are reported relative to a "bulk silicate Earth composition" and thus require subsequent renormalisation to NIST SRM 915a This renormalisation is a key step where a bias can easily be introduced relative to other lunar and terrestrial data measured directly relative to SRM 915a. This is pertinent because of the potential presence of a radiogenic ^{40}Ca anomaly on their "bulk silicate Earth" reference value relative to SRM 915a that could introduce a bias of 0.1‰ on renormalised $\delta^{44/40}$Ca (see Antonelli and Simon, 2020). The exact magnitude of a potential interlaboratory bias between the Simon and DePaolo (2010) and Simon et al. (2017) data and other studies is difficult to unequivocally demonstrate as the former present few data for other reference materials. Simon et al. (2017) report values for SRM 915b and BCR-2 that are, however, both on the high end of the range of published values (0.81 ± 0.18‰ and 0.87 ± 0.08‰, respectively; see Figure S2) yet not statistically distinct. Nevertheless, we think that a +0.1‰ interlaboratory bias in the Simon and DePaolo (2010) and Simon et al. (2017) data is the best explanation for the discrepancy. Such a bias would bring their data in good agreement with both our new results and the other studies reporting Ca isotope compositions of mare basalts.

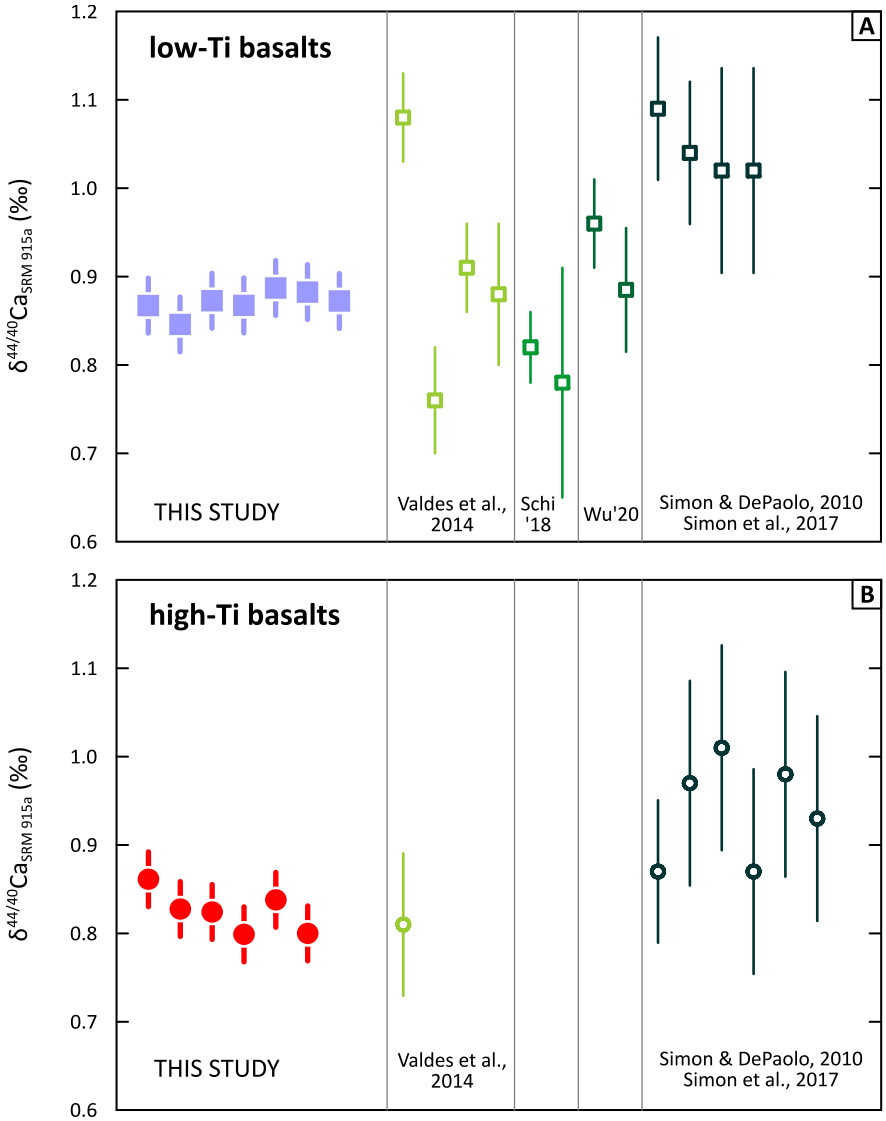

Figure S5. *Calcium isotope data ($\delta^{44/40}Ca$) for low- and high-Ti mare basalts from this study compared to previously published results (Simon and DePaolo, 2010; Valdes et al., 2014; Simon et al., 2017; Schiller et al., 2018; Wu et al., 2020).*

4. Low-pressure differentiation of the mare basalts

The mare basalts are not primary melts, but their compositions are variably modified by fractional crystallisation and, less commonly, crystal accumulation at low pressure. The liquid lines of descent of lunar basaltic magmas have been the topic of numerous experimental studies (see Longhi, 1992 for a summary and discussion) and are thus fairly well understood. Low-Ti magmas only crystallise olivine and minor Cr-spinel for a long interval (>100 °C) below the liquidus whereas magmas with higher TiO_2 contents typically have a short olivine-only crystallisation interval before reaching the olivine-armalcolite cotectic. Pyroxene and plagioclase are not present near the liquidus for any lunar magma composition at 1 atmosphere.

Calcium is incompatible in both olivine and armalcolite and as a result, CaO contents of the mare basalts are higher and more variable than those observed in primitive pyroclastic glasses (see also Figure 3 in the main text). We apply a correction for the effects of fractional crystallisation at low-pressure to the composition of the mare basalts in order to provide an estimate of the composition of their parental melts, which are used in the petrogenetic modelling, based on the experimentally-deduced liquid lines of descent. The main assumption in our approach is that the parental melts of the mare basalts overlap in composition with the primitive pyroclastic glasses in a MgO versus TiO_2 diagram, as indicated by the grey line in Figure S6a. For the low-Ti samples (including KREEP-rich basalt 15386), olivine was added incrementally until the bulk composition reached the MgO content of the assumed parental melt. Olivine was assumed to be in equilibrium with the melt using olivine–melt $K_D^{Fe\text{-}Mg}$ = 0.32 and K_D^{CaO} = 0.03. Low-Ti basalt 12040 has higher MgO content than the presumed parental melt composition and likely accumulated olivine, which is supported by the large proportion of modal olivine in the hand specimen (Hallis et al., 2014). For the high-Ti samples, armalcolite and olivine were added incrementally in a 58:42 proportion to reproduce the slope of the olivine+armalcolite cotectic in TiO_2-MgO space as borne out by high-Ti mare basalts and experimental studies (Longhi, 1992). Armalcolite was assumed to be Ca-free and have a $K_D^{Fe\text{-}Mg}$ = 0.79 (Longhi, 1987) whereas olivine was ascribed a lower $K_D^{Fe\text{-}Mg}$ of 0.28 due to the higher TiO_2 content of the melt (Xirouchakis et al., 2001). The bulk compositions were predicted to follow the olivine+armalcolite cotectic until they reached the highest TiO_2 content recorded in their suite (12 wt.% TiO_2 for Apollo 11 samples, 13.5 wt.% TiO_2 for Apollo 17 samples) after which olivine was the sole crystallising phase, again until the bulk composition reached the MgO content of the assumed parental melt (Figure S6). The Ca isotope effect of the removal of olivine was calculated using $\alpha_{olivine\text{-}melt}$ = 1.000374–1.000527 (see section 4 for details), which resulted in a marginal increase in $\delta^{44/40}Ca$ of the bulk composition (<0.01‰; Figure S6b). Note that armalcolite is assumed to be Ca-free and thus to have no leverage on $\delta^{44/40}Ca$.

Clearly, this correction for low-pressure fractional crystallisation has a notable effect on absolute major element concentrations but Al_2O_3/CaO, which is a key parameter in our arguments, is barely affected. For the low-Ti samples, TiO_2/CaO is equally unaffected, but the removal of armalcolite has a notable effect on TiO_2/CaO of the several high-Ti samples. The correction for low-pressure fractional crystallisation reduces the large range in measured TiO_2/CaO of the high-Ti samples (0.79-1.60) to two narrow clusters (1.02-1.10 for Apollo 11 samples, 1.17-1.24 for Apollo 17 samples). The major element composition and $\delta^{44/40}Ca$ of the mare basalt samples corrected low-pressure fractional crystallisation is given in supplementary Dataset 1.

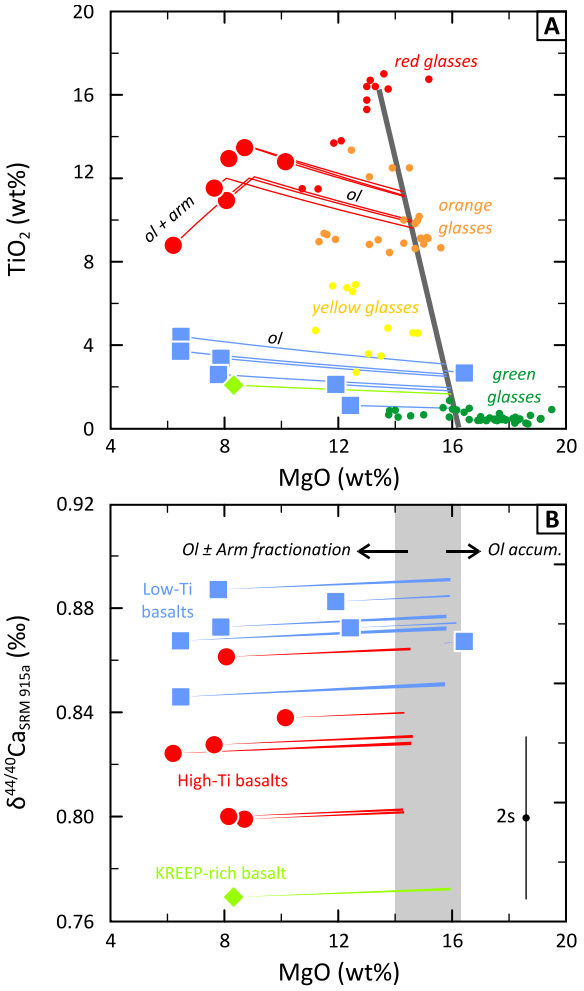

Figure S6. *The effects of low-pressure fractional crystallisation of olivine±armalcolite on the major element composition (A) and $\delta^{44/40}Ca$ (B) of the mare basalts; see text for discussion. Coloured lines show the modelled low-pressure liquid line of descent of the mare basalt samples; the grey line overlapping with the primitive pyroclastic glasses depcits the presumed compositions of mare basalt parental melts. Data for primitive pyroclastic glasses (green, yellow, orange and red) are from Delano (1986) and Shearer and Papike (1993).*

5. LMO crystallisation model

The crystallisation of the lunar magma ocean (LMO) has been studied extensively (e.g., Snyder et al., 1992; Elardo et al., 2011; Elkins-Tanton et al., 2011; Lin et al., 2017; Charlier et al., 2018; Rapp and Draper, 2018). In general, a similar crystallisation history emerges from these studies. We have opted to use the study of Charlier et al. (2018) as the basis for our modelling of the Ca isotope evolution during LMO solidification for two reasons: i) this study is the most detailed (i.e., most experiments and covering the entire solidification interval) for a LPUM bulk Moon composition (Longhi, 2006); and ii) Charlier et al. (2018) include a parameterisation of the composition of crystallising phases as a function of intensive parameters (P, T) and melt chemistry, thus enabling forward modelling of LMO solidification. To reiterate, all LMO solidification studies yield highly similar results and thus any of the other model is unlikely to show a notably different Ca isotope evolution and will not lead to different conclusions.

We have modelled two distinct LMO crystallisation scenarios with the transition from equilibrium- to fractional crystallisation occurring at 40% (FC model) and 70% (EC model) solidification. Note that the FC model with the EC–FC transition at 40% LMO solidification is essentially equivalent to a full fractional crystallisation scenario in the case of $\delta^{44/40}$Ca (Figure S7). The evolution of the composition of the melt and crystallising phases was calculated following the parameterisation of phase compositions of Charlier et al. (2018) in 0.5 wt.% (up to 60% LMO solidification) and 0.2 wt.% (60–99% LMO solidification) crystallisation increments. Hence, we approximate fractional crystallisation as 0.2 wt.% equilibrium crystallisation increments. Cotectic phase proportions were also taken from Charlier et al. (2018) but in some cases modified slightly to best reproduce the experimental LPUM liquid line of descent. The parameterisation of Charlier et al. (2018) lists a term for the temperature-dependence of pigeonite $K_D^{Fe\text{-}Mg}$ as "-0.000512T". This appears to be a typo in their supplemental file as such a negative temperature dependence does not reproduce their experimental data, whereas using "+0.000512T" does. Hence, we use the latter positive temperature dependence term. The two LMO crystallisation models are available in supplementary Dataset 2 where the major element composition of crystallising phases and residual melt is given as a function of percentage LMO solidification.

The instantaneous cumulates, which are in equilibrium with the residual melt in each crystallisation step, are divided in plagioclase and sinking instantaneous cumulates. The former is expected to float and form the lunar anorthosite crust whereas the latter comprise the phases with a density greater than the melt (olivine, pyroxene, ilmenite) that are presumed to sink and form the lunar cumulate mantle. In line with previous studies (e.g., Snyder et al., 1992; van Orman and Grove, 2000), we assume that the sinking instantaneous cumulates contain a small fraction (7 wt.%) of plagioclase that is trapped between the mafic phases.

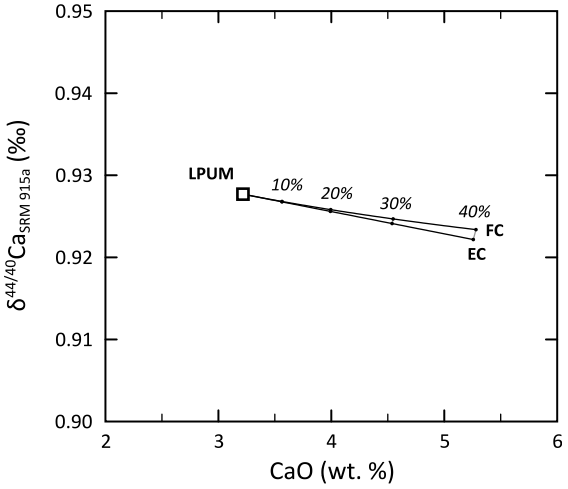

Figure S7. *The composition of the LMO residual melt during the first 40% of solidification (labels) during which olivine is the sole crystallising phase. The figure shows the negligble difference between fractional- (FC) and equilibrium crystallisation (EC).*

6. Ca isotope modelling of LMO crystallisation and cumulate remelting

The basis of the isotopic mass balance models in this paper are Ca isotope fractionation factors α between two phases (A and B), given by the following equation (see e.g., Young et al., 2015):

$$\alpha_{A-B} = \frac{(^{44}Ca/^{40}Ca)_A}{(^{44}Ca/^{40}Ca)_B} = \frac{\beta_A}{\beta_B} \quad (Eq. 1)$$

In this equation, β is the reduced partition function ratio. The value of $^{44}Ca/^{40}Ca$ for a phase is relative to $^{44}Ca/^{40}Ca$ = 0.0212076 for NIST SRM 915a. We use reduced partition function ratios for the Ca-bearing minerals in the lunar mantle that are derived from *ab initio* density functional theory calculations as reported by Huang et al. (2019), listed in Table S2 and shown in Figure S8. These Ca isotope fractionation factors agree well with those in the *ab initio* study of Antonelli et al. (2019), but because the latter do not include results for pigeonite, we use the values of Huang et al. (2019) for sake of consistency. No *ab initio* reduced partition function ratio is available for ilmenite and hence we assign a value of 1 to $\alpha_{ilmenite\text{-}melt}$. Given the very low CaO content of ilmenite (<0.42 wt.%) and its late appearance as a crystallising phase, any bias in this value will have at most a marginal effect on our Ca isotope model of LMO solidification and is unlikely to change any of the conclusions in this paper. The reduced partition function ratio of a melt phase cannot be calculated from first principles and hence we employ the empirical augite-melt Ca isotope fractionation factor found by Zhang et al. (2018), which is based on a regression of Ca isotope data for samples from the Kilauea Iki lava lake:

$$\Delta^{44/40}Ca_{augite-melt} = \frac{0.09 \pm 0.07}{(T/1000)^2} \quad (Eq. 2)$$

The uncertainty on the augite-melt fractionation factor in Equation 2 is propagated throughout our LMO crystallisation and cumulate re-melting modelling. We combine the *ab initio* mineral-mineral reduced partition function ratios with the empirical augite-melt fractionation factor through the approximation that is valid for a value of α near unity:

$$\Delta^{44/40}Ca_{A-B} \approx 1000 ln\alpha_{A-B} \quad (Eq. 3)$$

This gives us a set of temperature-dependent reduced partition function ratios for all phases. Figure S8 shows the Ca isotope fractionation factors for all phases relative to augite, reported as $\Delta^{44/40}Ca_{i\text{-}aug}$ to allow easy comparison to $\delta^{44/40}Ca$ values. This figure indicates that olivine, orthopyroxene and clinopyroxene (pigeonite and augite) are isotopically heavy (higher $\delta^{44/40}Ca$) relative to the melt, whereas plagioclase marginally overlaps on the isotopically light side with the melt.

To assess the accuracy of these Ca isotope fractionation factors, we have tested whether they can reproduce the observed difference in $\delta^{44/40}Ca$ between fertile peridotite (0.928 ± 0.009‰; 95% confidence interval) and MORB (0.863 ± 0.018‰; 95% confidence interval) shown in Figure 1 in the manuscript. Details on the isotopic mass balance equations used to calculate the composition of partial melts is given below. Figure S9 shows that the $\Delta^{44/40}Ca_{melt\text{-}source}$ of batch melts of a primitive mantle composition at 1 and 2 GPa overlap with the observed $\Delta^{44/40}Ca_{MORB\text{-}PM}$. Although the generation of MORB is a more complex process than batch melting, the marginal variation in $\Delta^{44/40}Ca_{melt\text{-}source}$ as a function of degree of melting and pressure for clinopyroxene-saturated melts suggests that other melting styles (e.g., fractional melting, polybaric melting) are unlikely to yield significantly different results.

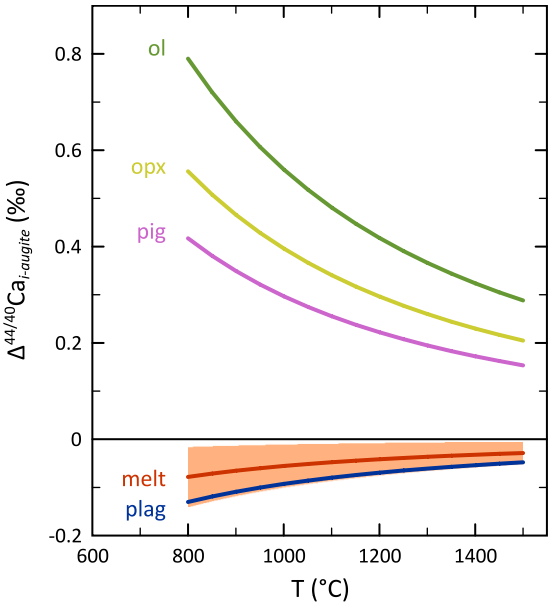

Figure S8. *Temperature-dependent Ca isotope fractionation factor between phase i and augite used in this study. Mineral-mineral fractionation factors are from the first principles as reported by Huang et al. (2019); the augite-melt fractionation factor with uncertainty envelope is from Zhang et al. (2018).*

Table S3. *Fitting parameters for reduced partition function ratios (1000lnβ) after Huang et al. (2019).*

phase	formula	a	b	c
forsterite	$Ca_{1/32}Mg_{63/32}SiO_4$	0	0	2.362
orthopyroxene	$Ca_{1/48}Mg_{47/48}SiO_3$	$1.94 \cdot 10^{-4}$	$-1.32 \cdot 10^{-2}$	2.104
pigeonite	$Ca_{1/8}Mg_{7/8}SiO_3$	$1.15 \cdot 10^{-4}$	$-1.11 \cdot 10^{-2}$	1.942
augite	$CaMgSi_2O_6$	$1.18 \cdot 10^{-4}$	$-6.89 \cdot 10^{-3}$	1.458
plagioclase	$CaAl_2Si_2O_8$	$6.21 \cdot 10^{-5}$	$-5.68 \cdot 10^{-3}$	1.307

$1000\ ln\beta = ax^3+bx^2+cx$, where $x = 10^6/T^2$, with T in Kelvin.

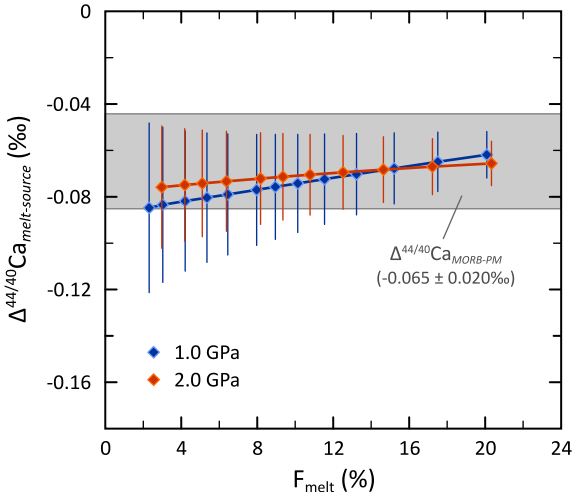

Figure S9. *Isotopic fractionation between a batch melt and its mantle source ($\Delta^{44/40}Ca_{mantle\text{-}source}$) as a function of degree of melting and pressure, based on pMELTS models of melting a primitive mantle composition (Palme and O'Neill, 2014). The shaded grey field is the observed difference in $\delta^{44/40}Ca$ between MORB and fertile peridotites ($\Delta^{44/40}Ca_{MORB\text{-}PM}$ = -0.065 ± 0.020‰; 95% confidence interval; based on the data shown in Figure 1 in the manuscript).*

Equilibrium isotopic fractionation is governed by a mass balance equation identical to the mixing equation for radiogenic isotope systems:

$$\bar{R} = \frac{C_{melt}F_{melt}R_{melt} + C_{ol}F_{ol}R_{ol} + C_{opx}F_{opx}R_{opx} + \cdots}{\bar{C}} \quad (Eq. 4)$$

In which R is an isotopic ratio, $^{44}Ca/^{40}Ca$ in this case (relative to $^{44}Ca/^{40}Ca = 0.0212076$ for NIST SRM 915a), C the element concentration and F the proportion of a phase. The bar symbol indicates the bulk isotopic composition or Ca concentration of the system. If we define α_i as the ratio of the isotopic compositions of phase *i* and the melt:

$$\alpha_i = \frac{R_i}{R_{melt}} \quad (Eq. 5)$$

The isotopic mass balance equation can be written as a function of the isotopic composition of the melt:

$$\bar{R} = \frac{C_{melt}F_{melt}R_{melt}\alpha_{melt} + C_{ol}F_{ol}R_{melt}\alpha_{ol} + C_{opx}F_{opx}R_{melt}\alpha_{opx} + \cdots}{\bar{C}} \quad (Eq. 6)$$

And rewritten as:

$$\bar{R} = \frac{R_{melt}\sum_i(C_iF_i\alpha_i)}{\bar{C}} \quad (Eq. 7)$$

When the bulk isotopic composition is known, the isotopic composition of the melt is obtained by rearranging the equation:

$$R_{melt} = \frac{\bar{R}\bar{C}}{\sum_i(C_iF_i\alpha_i)} \quad (Eq. 8)$$

And:

$$\delta^{44/40}Ca_{melt} = \left[\frac{R_{melt}}{R_{SRM\ 915a}}\right] - 1 \quad (Eq. 9)$$

These are the fundamental equations that are used to calculate the Ca isotope composition of the residual melt and crystallising phases during LMO crystallisation, and the composition of the melt and residue during subsequent re-melting of cumulate reservoirs. For LMO crystallisation, the phase proportions and Ca content of each phase are provided by the LMO crystallisation models (section 5); for cumulate re-melting these are given by the pMELTS models. The values for $\alpha_{i\text{-melt}}$ are calculated for each crystallisation or melting step at the temperature given by the LMO crystallisation or pMELTS models.

Cumulate re-melting Ca isotope mass balance calculations are based on the pMELTS models, which were run in 5 °C increments from the liquidus to the solidus. The Ca isotope composition of the partial melts was calculated through the mass balance equation described above for the interval 0.5–10 wt.% melting (see supplementary Dataset 3). Due to the petrological evidence for a clinopyroxene-free mantle source for the mare basalts (e.g., Longhi, 1992), we only considered pMELTS results that did not have residual clinopyroxene (augite or pigeonite) in that melt fraction interval. In order to obtain $\delta^{44/40}Ca$ values for a constant degree of melting between models (Figures 4, 5 and 7 in the main manuscript), we regressed $\delta^{44/40}Ca \pm 2s$, CaO content, Al_2O_3/CaO and TiO_2/CaO of the melt as a function of melt fraction as a cubic polynomial. These parameters yielded good fits with an R^2 generally >0.95.

7. P and fO_2 dependence of pMELTS models

Modelling of partial melting of various cumulate compositions was undertaken using pMELTS (version 5.6.1; Ghiorso et al., 2002) with the MELTS for Excel front end graphical user interface (version 2018Apr2; Gualda and Ghiorso, 2015). All models shown in the main manuscript were run at a pressure of 2.0 GPa and fO_2 = IW. Dependence of the partial melt compositions was investigated for a representative hybrid cumulate composition and shown in Figure S10.

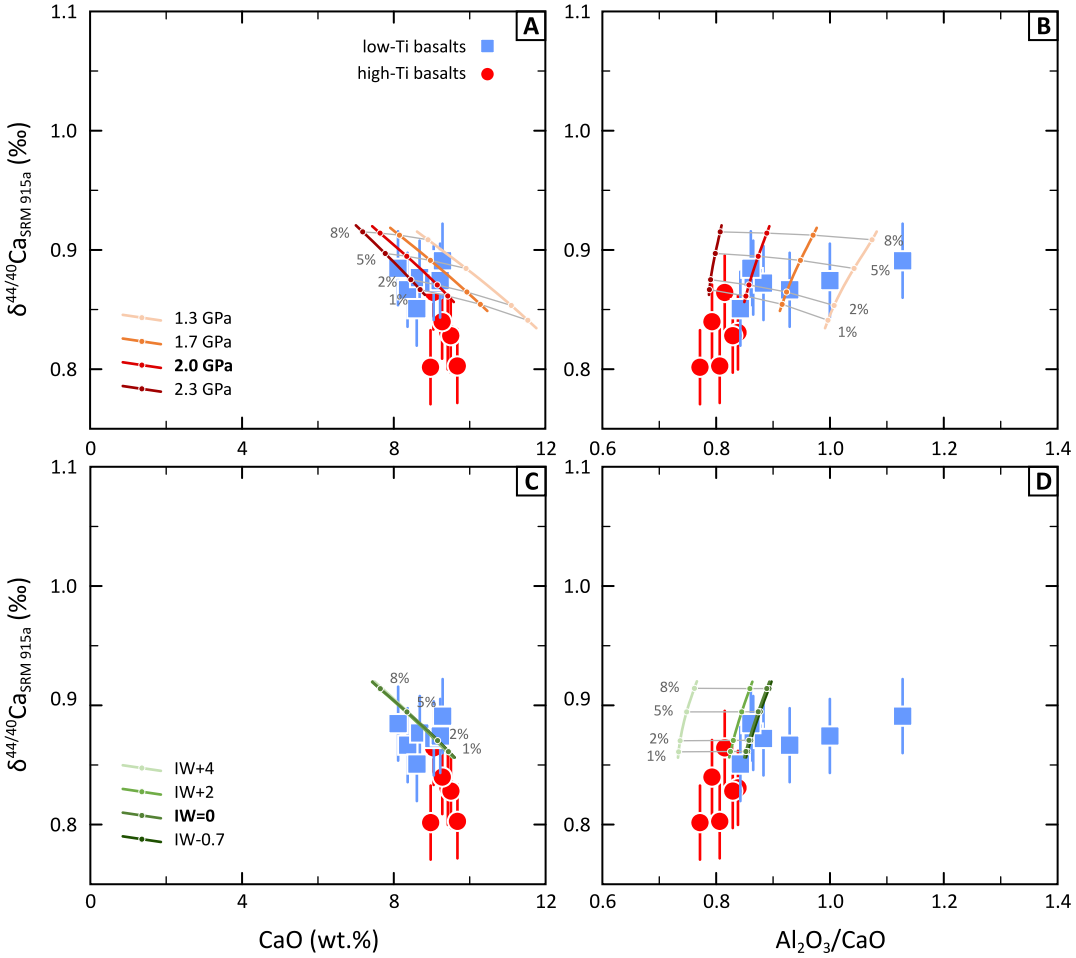

Figure S10. *Dependence of the pMELTS model of a hybrid cumulate composition (EC74 + 10% EC95) on pressure (a and b) and oxygen fugacity (c and d). All models in the main manuscript were run at a pressure of 2.0 GPa and oxygen fugacity at the iron-wüstite (IW) buffer. Neither varying pressure nor fO_2 has a notable influence on $\delta^{44/40}Ca$ of the partial melts, but Al_2O_3/CaO shows some dependence on pressure. At an oxygen fugacity lower than ~IW-0.7, pMELTS predicts the presence of metallic Fe with an impossible composition (e.g., -286 wt.% Fe_2O_3 and 386 wt.% FeO).*

References

Albarède, F., Beard, B., 2004. Analytical methods for non-traditional isotopes. Rev. Mineral. Geochem. 55, 113-152.

Amini, M., Eisenhauer, A., Böhm, F., Holmden, C., Kreissig, K., Hauff, F., Jochum, K.P., 2009. Calcium isotopes (δ44/40Ca) in MPI-DING reference glasses, USGS rock powders and various rocks: Evidence for Ca isotope fractionation in terrestrial silicates. Geostand. Geoanal. Res. 33, 231-247.

Amsellem, E., Moynier, F., Pringle, E.A., Bouvier, A., Chen, H., Day, J.M., 2017. Testing the chondrule-rich accretion model for planetary embryos using calcium isotopes. Earth Planet. Sci. Lett. 469, 75-83.

Antonelli, M.A., Schiller, M., Schauble, E.A., Mittal, T., DePaolo, D.J., Chacko, T., Grew, E.S., Tripoli, B., 2019. Kinetic and equilibrium Ca isotope effects in high-T rocks and minerals. Earth Planet. Sci. Lett. 517, 71-82.

Antonelli, M.A., Simon, J.I., 2020. Calcium isotopes in high-temperature terrestrial processes. Chem. Geol. 548, 119651.

Bevan, D., Coath, C.D., Lewis, J., Schwieters, J., Lloyd, N., Craig, G., Wehrs, H., Elliott, T., 2021. In situ Rb–Sr dating by collision cell, multicollection inductively-coupled plasma mass-spectrometry with pre-cell mass-filter (CC-MC-ICPMS/MS). J. Anal. At. Spectrom.

Caro, G., Papanastassiou, D., Wasserburg, G., 2010. 40K–40Ca isotopic constraints on the oceanic calcium cycle. Earth Planet. Sci. Lett. 296, 124-132.

Charlier, B., Grove, T.L., Namur, O., Holtz, F., 2018. Crystallization of the lunar magma ocean and the primordial mantle-crust differentiation of the Moon. Geochim. Cosmochim. Acta 234, 50-69.

Chen, C., Ciazela, J., Li, W., Dai, W., Wang, Z., Foley, S.F., Li, M., Hu, Z., Liu, Y., 2020. Calcium isotopic compositions of oceanic crust at various spreading rates. Geochim. Cosmochim. Acta 278, 272-288.

Chen, C., Dai, W., Wang, Z., Liu, Y., Li, M., Becker, H., Foley, S.F., 2019. Calcium isotope fractionation during magmatic processes in the upper mantle. Geochim. Cosmochim. Acta 249, 121-137.

Delano, J.W., 1986. Pristine lunar glasses: Criteria, data, and implications. Journal of Geophysical Research: Solid Earth 91, 201-213.

DePaolo, D.J., 2004. Calcium isotopic variations produced by biological, kinetic, radiogenic and nucleosynthetic processes. Rev. Mineral. Geochem. 55, 255-288.

Eiden, G.C., Barinaga, C.J., Koppenaal, D.W., 1996. Communication. Selective removal of plasma matrix ions in plasma source mass spectrometry. J. Anal. At. Spectrom. 11, 317-322.

Elardo, S.M., Draper, D.S., Shearer Jr, C.K., 2011. Lunar Magma Ocean crystallization revisited: Bulk composition, early cumulate mineralogy, and the source regions of the highlands Mg-suite. Geochim. Cosmochim. Acta 75, 3024-3045.

Elkins-Tanton, L.T., Burgess, S., Yin, Q.-Z., 2011. The lunar magma ocean: Reconciling the solidification process with lunar petrology and geochronology. Earth Planet. Sci. Lett. 304, 326-336.

Feng, L.p., Zhou, L., Yang, L., DePaolo, D.J., Tong, S.Y., Liu, Y.S., Owens, T.L., Gao, S., 2017. Calcium isotopic compositions of sixteen USGS reference materials. Geostand. Geoanal. Res. 41, 93-106.

Ghiorso, M.S., Hirschmann, M.M., Reiners, P.W., Kress III, V.C., 2002. The pMELTS: A revision of MELTS for improved calculation of phase relations and major element partitioning related to partial melting of the mantle to 3 GPa. Geochem. Geophys. Geosyst. 3, 1-35.

Gualda, G.A., Ghiorso, M.S., 2015. MELTS _ Excel: A Microsoft Excel-based MELTS interface for research and teaching of magma properties and evolution. Geochem. Geophys. Geosyst. 16, 315-324.

Hallis, L., Anand, M., Strekopytov, S., 2014. Trace-element modelling of mare basalt parental melts: implications for a heterogeneous lunar mantle. Geochim. Cosmochim. Acta 134, 289-316.

He, Y., Wang, Y., Zhu, C., Huang, S., Li, S., 2017. Mass-independent and mass-dependent Ca isotopic compositions of thirteen geological reference materials measured by thermal ionisation mass spectrometry. Geostand. Geoanal. Res. 41, 283-302.

Heuser, A., Eisenhauer, A., 2008. The calcium isotope composition (δ44/40Ca) of NIST SRM 915b and NIST SRM 1486. Geostand. Geoanal. Res. 32, 27-32.

Hogmalm, K.J., Zack, T., Karlsson, A.K.-O., Sjöqvist, A.S., Garbe-Schönberg, D., 2017. In situ Rb–Sr and K–Ca dating by LA-ICP-MS/MS: an evaluation of N 2 O and SF 6 as reaction gases. J. Anal. At. Spectrom. 32, 305-313.

Holmden, C., 2005. Measurement of δ44Ca Using a 43Ca-42Ca Double-spike TIMS. Saskat. Geol. Surv 1.

Holmden, C., Bélanger, N., 2010. Ca isotope cycling in a forested ecosystem. Geochim. Cosmochim. Acta 74, 995-1015.

Horwitz, E.P., Chiarizia, R., Dietz, M.L., 1992. A novel strontium-selective extraction chromatographic resin. Solvent extraction and ion exchange 10, 313-336.

Huang, F., Zhou, C., Wang, W., Kang, J., Wu, Z., 2019. First-principles calculations of equilibrium Ca isotope fractionation: Implications for oldhamite formation and evolution of lunar magma ocean. Earth Planet. Sci. Lett. 510, 153-160.

Kang, J.-T., Ionov, D.A., Liu, F., Zhang, C.-L., Golovin, A.V., Qin, L.-P., Zhang, Z.-F., Huang, F., 2017. Calcium isotopic fractionation in mantle peridotites by melting and metasomatism and Ca isotope composition of the Bulk Silicate Earth. Earth Planet. Sci. Lett. 474, 128-137.

Klaver, M., Coath, C., 2019. Obtaining accurate isotopic compositions with the double spike technique: practical considerations. Geostand. Geoanal. Res. 43, 5-22.

Lewis, J., Luu, T-H., Coath, C. D., Wehrs, H., Schwieters, J. B. and Elliott, T, 2021. Collision Course: High precision mass independent and mass dependent calcium isotope measurements using the prototype collision cell MC-ICPMS/MS, Proteus. Invited manuscript in preparation for submission to Chem. Geol.

Li, X., Han, G., 2021. One-step chromatographic purification of K, Ca, and Sr from geological samples for high precision stable and radiogenic isotope analysis by MC-ICP-MS. J. Anal. At. Spectrom. 36, 676-684.

Lin, Y., Tronche, E.J., Steenstra, E.S., van Westrenen, W., 2017. Evidence for an early wet Moon from experimental crystallization of the lunar magma ocean. Nat. Geosci. 10, 14-18.

Longhi, J., 1987. On the connection between mare basalts and picritic volcanic glasses. Journal of Geophysical Research: Solid Earth 92, E349-E360.

Longhi, J., 1992. Experimental petrology and petrogenesis of mare volcanics. Geochim. Cosmochim. Acta 56, 2235-2251.

Longhi, J., 2006. Petrogenesis of picritic mare magmas: constraints on the extent of early lunar differentiation. Geochim. Cosmochim. Acta 70, 5919-5934.

Nier, A.O., 1938. The isotopic constitution of strontium, barium, bismuth, thallium and mercury. Physical Review 54, 275-278.

Palme, H., O'Neill, H., 2014. Cosmochemical estimates of mantle composition, in: Holland, H.D., Turekian, K.K. (Eds.), Treatise on geochemistry (2nd edition). Elsevier, Oxford, pp. 1-39.

Rapp, J., Draper, D., 2018. Fractional crystallization of the lunar magma ocean: Updating the dominant paradigm. Meteorit. Planet. Sci. 53, 1432-1455.

Rudge, J.F., Reynolds, B.C., Bourdon, B., 2009. The double spike toolbox. Chem. Geol. 265, 420-431.

Russell, W., Papanastassiou, D., Tombrello, T., 1978. Ca isotope fractionation on the Earth and other solar system materials. Geochim. Cosmochim. Acta 42, 1075-1090.

Schiller, M., Bizzarro, M., Fernandes, V.A., 2018. Isotopic evolution of the protoplanetary disk and the building blocks of Earth and the Moon. Nature 555, 507-510.

Sedaghatpour, F., Jacobsen, S.B., 2019. Magnesium stable isotopes support the lunar magma ocean cumulate remelting model for mare basalts. Proceedings of the National Academy of Sciences 116, 73-78.

Shearer, C., Papike, J., 1993. Basaltic magmatism on the Moon: A perspective from volcanic picritic glass beads. Geochim. Cosmochim. Acta 57, 4785-4812.

Simon, J., Jordan, M., Tappa, M., Schauble, E., Kohl, I., Young, E., 2017. Calcium and titanium isotope fractionation in refractory inclusions: Tracers of condensation and inheritance in the early solar protoplanetary disk. Earth Planet. Sci. Lett. 472, 277-288.

Simon, J.I., DePaolo, D.J., 2010. Stable calcium isotopic composition of meteorites and rocky planets. Earth Planet. Sci. Lett. 289, 457-466.

Snyder, G.A., Taylor, L.A., Neal, C.R., 1992. A chemical model for generating the sources of mare basalts: Combined equilibrium and fractional crystallization of the lunar magmasphere. Geochim. Cosmochim. Acta 56, 3809-3823.

Steiger, R.H., Jäger, E., 1977. Subcommission on geochronology: convention on the use of decay constants in geo-and cosmochronology. Earth Planet. Sci. Lett. 36, 359-362.

Valdes, M.C., Moreira, M., Foriel, J., Moynier, F., 2014. The nature of Earth's building blocks as revealed by calcium isotopes. Earth Planet. Sci. Lett. 394, 135-145.

van Orman, J.A., Grove, T.L., 2000. Origin of lunar high-titanium ultramafic glasses: Constraints from phase relations and dissolution kinetics of clinopyroxene-ilmenite cumulates. Meteorit. Planet. Sci. 35, 783-794.

Wu, W., Xu, Y.-G., Zhang, Z.-F., Li, X., 2020. Calcium isotopic composition of the lunar crust, mantle, and bulk silicate Moon: A preliminary study. Geochim. Cosmochim. Acta 270, 313-324.

Xirouchakis, D., Hirschmann, M.M., Simpson, J.A., 2001. The effect of titanium on the silica content and on mineral-liquid partitioning of mantle-equilibrated melts. Geochim. Cosmochim. Acta 65, 2201-2217.

Young, E.D., Manning, C.E., Schauble, E.A., Shahar, A., Macris, C.A., Lazar, C., Jordan, M., 2015. High-temperature equilibrium isotope fractionation of non-traditional stable isotopes: Experiments, theory, and applications. Chem. Geol. 395, 176-195.

Zhang, H., Wang, Y., He, Y., Teng, F.Z., Jacobsen, S.B., Helz, R.T., Marsh, B.D., Huang, S., 2018. No measurable calcium isotopic fractionation during crystallization of Kilauea Iki lava lake. Geochem. Geophys. Geosyst. 19, 3128-3139.

Zhu, H., Du, L., Li, X., Zhang, Z., Sun, W., 2020. Calcium isotopic fractionation during plate subduction: Constraints from back-arc basin basalts. Geochim. Cosmochim. Acta 270, 379-393.

Zhu, H., Liu, F., Li, X., Wang, G., Zhang, Z., Sun, W., 2018. Calcium isotopic compositions of normal Mid-Ocean Ridge basalts from the southern Juan de Fuca Ridge. Journal of Geophysical Research: Solid Earth 123, 1303-1313.